

EXPERIMENTAL DETERMINATION OF THE
FOUR PRINCIPAL DRAG COEFFICIENTS OF
MAGNETOSPIRILLUM MAGNETICUM
AMB-1 CELLS

EXPERIMENTAL DETERMINATION OF THE FOUR
PRINCIPAL DRAG COEFFICIENTS OF *MAGNETOSPIRILLUM*
MAGNETICUM AMB-1 CELLS

BY
LIU YU, B.Sc.

A THESIS
SUBMITTED TO THE DEPARTMENT OF ENGINEERING
AND THE SCHOOL OF GRADUATE STUDIES
OF MCMASTER UNIVERSITY
IN PARTIAL FULFILMENT OF THE REQUIREMENTS
FOR THE DEGREE OF
MASTER OF APPLIED SCIENCE

© Copyright by Liu Yu, July 2020

All Rights Reserved

Master of Applied Science (2020)
(Engineering)

McMaster University
Hamilton, Ontario, Canada

TITLE: Experimental Determination of the Four Principal Drag
Coefficients of *Magnetospirillum magneticum* AMB-1
cells

AUTHOR: Liu Yu
B.Sc. (Mathematical Physics),
University of Waterloo, Waterloo, Canada
B.Sc. (Mathematics and Applied Mathematics),
China University of Geosciences, Wuhan, China

SUPERVISOR: Dr. Cécile Fradin

NUMBER OF PAGES: xiv, 83

Abstract

Magnetotactic bacteria (MTB) possess organelles called magnetosomes which contain magnetite (Fe_3O_4) or greigite (Fe_3S_4) nanocrystals. These particles generate a magnetic moment allowing the use of external magnetic fields to control the cell orientation. MTB use this magnetic moment to reach environments with optimal oxygen concentration, a process called magnetotaxis. There are many possible technological applications for MTB, for example, they have been used as nanorobots to push beads and they can be used to remove heavy metals and radionuclides from waste water. In order to fully understand the motion of these micron-size organisms, which takes place at very low Reynolds number where friction dominates over inertia, we set out to measure their drag coefficients. As a starting point, we used a well-studied species of MTB with a corkscrew shape, *Magnetospirillum magneticum* AMB-1. Simulations were done to find the best external magnetic field strength at which to observe their diffusion. We then imaged non-motile cells placed in these preferred uniform magnetic fields and used automated image analysis to determine the position and orientation of the cells in each frame. This allowed calculating orientation correlation functions and mean-squared displacements, from which rotational and translational diffusion coefficients were obtained for each individual cell. We observed that the four principal drag coefficients of these cells greatly vary as a function of cell length as predicted for

cylindrical or elliptical objects with comparable radius. However, we also detecting a coupling between the rotation around and translation along the long axis of the cell only observed for chiral objects. We were able for the first time to experimentally fully characterize the friction matrix for a micron-size elongated chiral object.

Continuing our work on MTB, to study live cells for long periods of time, we looked to confine them in PDMS nanowells, but found that MTB were not growing well in this environment. We then turned to a device, which incorporated a PDMS microchannel to provide continuous nutrients and a gel membrane to enable cellular growth into a 2D monolayer. Hopefully, this experimental setup combined with time-lapse microscopy can in the future be used to observe cell growth and cell division, and further to determine whether the magnetosome of the mother is passed on equally between daughter cells.

Preface

The goal of my thesis was to study some physical aspects of the swimming motion of magnetotactic bacteria. This thesis starts with an introduction chapter that provides a general background on magnetotactic bacteria and their motion, and introduces the *Magnetospirillum magneticum* bacterial strain used in this study. In the second chapter, the methods used to perform the simulations, the experiments and the analysis are detailed. In chapter 3, the central part of the thesis, the results of the drag coefficient measurements are presented and discussed. Chapter 4 includes preliminary results on the growth of magnetotactic bacteria in microfluidic devices which we are planning to use to study cell growth and division. The last chapter is a general conclusion of the work presented in the thesis.

Acknowledgements

I had a rewarding two-year MASc experience at McMaster, during which I have been lucky to be helped by many wonderful people.

First of all, I would like to thank my supervisor Dr. Cécile Fradin. Cécile, thank you for all the advice and suggestions, I have learned so much from you not only academically. Thank you for giving me the opportunity to work with our fascinating MTB. In addition, I really love the simulation experience - all the discussions we had, all the nights with my laptop running, and the simulation progress made every time. It has been a pleasure working with you!

I would also like to thank the past and present members in the Fradin group. Lucas, thank you for your patience and all the help you provided. It would take me a lot longer to learn how to culture MTB and how to use the microscopy without you. Ahmad, you made these two years really fun not only in the lab, at the 6I and 707 classes, but also the at gym classes. Michael, thank you for sharing your office with me at the beginning and your help with the microscopy and everything I need to find. Markus, thank you for teaching me how to align the microscopy and how to get rid of the grease on the objective. Carmina, thank you for your suggestions on choosing projects and the future path.

I would like to extend my thanks to Dr. P. Ravi Selvaganapathy and his lab,

particularly Shadi, for their expertise and help in the microfluidic realm. I also want to thank Dr. Ishwar K. Puri for taking valuable time to serve on my committee.

My office-mates, floor-mates, BME classmates and all my friends, you helped me when I was stressed and in difficulties. I really appreciate that. I would like to thank my parents and my family back in China for your support, encouragement and patience and most of all, your belief in me. Last but not least, I want to thank Xingzhi. You are such a good listener and a good advice-provider, and you always know what I need exactly. Thank you for your support, patience, help and most importantly, being there for me all the time!

Contents

Abstract	iii
Preface	v
Acknowledgements	vi
1 Introduction	1
1.1 Magnetotactic bacteria	1
1.1.1 Discovery of magnetotactic bacteria	1
1.1.2 Ecology, distribution and diversity of magnetotactic bacteria .	2
1.1.3 Structural properties - magnetosomes	5
1.1.4 Applications of magnetotactic bacteria	7
1.1.5 <i>Magnetospirillum magneticum</i> AMB-1	9
1.2 Motion of MTB	10
1.2.1 Life at low Reynolds number	10
1.2.2 Swimming behavior - propulsive forces	13
1.2.3 Thermal forces and diffusion	15
1.2.4 Drag coefficients	17
1.2.5 Interaction with a magnetic field	19

2	Methods	22
2.1	Simulations of rotational diffusion	22
2.2	Cell culture	24
2.2.1	Growth medium	24
2.2.2	The racetrack method	25
2.2.3	Increasing cell length	26
2.3	Movie acquisition	27
2.4	Cell tracking	29
2.5	Orientation correlation functions	31
2.6	Limitations	32
3	Results and Discussion	33
3.1	Simulations results - measuring the rotational diffusion coefficients of cells from angular trajectories	34
3.1.1	Orientation distributions	34
3.1.2	Orientation correlation functions	37
3.1.3	Effect of measurement error	41
3.1.4	Effect of a misalignment between cell axis and magnetic moment	42
3.2	Experimental determination of <i>M. magneticum</i> rotational drag coeffi- cients	47
3.2.1	Rotation perpendicular to the cell longitudinal axis	47
3.2.2	Rotation around the cell longitudinal axis	50
3.3	Experimental determination of <i>M. magneticum</i> translational drag co- efficients	52

3.4	Coupling between rotation and translation along the cell longitudinal axis	56
3.4.1	Handedness of <i>M. magneticum</i> cells	56
3.4.2	Experimental detection of coupling between the rotation around and translation along the cell longitudinal axis	58
3.5	Comparison of different drag coefficients	59
4	Growing Magnetotactic Bacteria in Confined Environments	62
4.1	PDMS nanowells	63
4.2	PDMS microchannel with a gel membrane	67
5	Conclusion	70

List of Figures

1.1	Phylogenetic distribution of magnetotactic bacteria	3
1.2	Magnetosome chain assembly	5
1.3	Mechanisms of magnetosome biogenesis	6
1.4	TEM picture of an AMB-1 cell	9
1.5	Structure of Gram-negative bacterial flagellum	14
1.6	AMB-1 cell body and flagellar rotation directions	15
1.7	Diffusion of a particle released at x_0 at time 0	16
1.8	Linear relationship between MSD and time	17
1.9	Passive alignment with magnetic field	20
2.1	Orientation of the cell	22
2.2	Growth curve of a culture	24
2.3	Illustration of the racetrack method	26
2.4	Cell length distributions	27
2.5	Experimental setup	28
2.6	Home-built observation chamber	29
2.7	Illustration of the image analysis process	29
2.8	Three-dimensional model of a <i>M. magneticum</i> cell	30
3.1	Orientation trajectories and distributions from simulations	36

3.2	Results for rotation perpendicular to the cell longitudinal axis	39
3.3	Results for rotation parallel to the cell longitudinal axis	40
3.4	Influence of measurement noise on the OCF	41
3.5	Influence of a misalignment between the cell longitudinal axis \vec{L} and its magnetic moment $\vec{\mu}$	42
3.6	Results of simulations done for cells with different misalignment angles for rotation perpendicular to the cell longitudinal axis	44
3.7	Results of simulations with different misalignment angles for rotation parallel to the cell longitudinal axis	46
3.8	Examples of orientation distribution and OCF for rotation perpendic- ular to the cell longitudinal axis for two cells of different lengths . . .	47
3.9	Experimentally determined values of the rotational drag coefficient per- pendicular to the longitudinal axis of <i>M. magneticum</i> cells	49
3.10	Examples of orientation distribution and OCF for rotation around the cell longitudinal axis for two cells of different lengths	50
3.11	Experimentally determined values of the rotational drag coefficient around the longitudinal axis of <i>M. magneticum</i> cells	52
3.12	Translational diffusion	54
3.13	Experimentally determined translational drag coefficients of <i>M. mag- neticum</i> cells	55
3.14	Right- and left-handed helices	56
3.15	z - stack images	57
3.16	Results of coupling between rotation and translation	59
3.17	Dependence of drag coefficients on cell length	59

4.1	PDMS nanowell device	63
4.2	PDMS nanowell shape change	64
4.3	Number of cells in a single well vs. the relative cell concentration of the solution used to fill the wells on day 0	65
4.4	Images of cells in the wells	66
4.5	Schematic representation of PDMS microchannel with a gel membrane	67
4.6	Images of the microchannel and cells embedded on the gel surface . .	69

List of Tables

1.1	Drag coefficients of objects with different shapes	18
3.1	The four principal diffusion coefficients of an elongated object	37

Chapter 1

Introduction

1.1 Magnetotactic bacteria

1.1.1 Discovery of magnetotactic bacteria

The first paper mentioning magnetotactic bacteria (MTB) was written by Blakemore in 1975, in which he named the phenomenon of bacterial response to magnetic fields “magnetotaxis” [1]. While isolating *Spirochaeta plicatilis* from marine marsh muds collected from a pond in Woods Hole, Massachusetts, he observed microorganisms that migrated persistently northward in the earth magnetic field. Electron microscopy was used to show that these cells contain iron-rich crystals within membrane vesicles, which he suggested were responsible for the magnetotaxis behavior. He proposed that the magnetotactic mechanism is the combination of cell active swimming motion and cell body passive alignment with the geomagnetic field.

However, according to Frankel, in 1963, an Italian scientist called Salvatore Bellini had discovered “magneto-sensitive bacteria” but he didn’t get the permission from the

University of Pavia (Italy) to submit the manuscript [2]. In 2009, the manuscript was translated from Italian to English and then published [3]. In his study, he observed bacteria of various morphologies in freshwater samples that swam persistently northwards and accumulated at the north edge of water drops. In addition, he put one hanging drop of biological sample to the south and the second hanging drop of sterilized water to the north, and the microorganisms migrated to the drop of sterilized water. This method was then used to separate the microorganisms. Based on his observations, he hypothesized that the bacteria have an internal compass to direct them according to the magnetic field.

1.1.2 Ecology, distribution and diversity of magnetotactic bacteria

Magnetotactic bacteria are gram-negative, motile prokaryotes. They are ubiquitous in sediments of various environments including freshwater, brackish, marine and hypersaline habitats, and they have been found on all continents [4, 5]. It has been found that most of those in the north hemisphere were north-seeking and most of those in the south hemisphere were south-seeking. In addition, close to the geomagnetic equator, MTB cells are divided about equally between north- and south-seekers [6]. MTB are microaerophilic bacteria, which means they need dissolved O_2 to survive, but the O_2 concentration required is lower than the atmospheric oxygen concentration. The oxygen preference of MTB explains why they are mostly found in proximity to the oxic-anoxic interface (OAI) [5, 7]. Because they prefer slightly different chemical conditions, different species of magnetotactic bacteria occupy different positions within the OAI. Magnetite (Fe_3O_4) and greigite (Fe_3S_4) are two magnetic minerals

known to be biomineralized by MTB. The magnetite producers are found at the OAI while the greigite-producing MTB are found just below the OAI where the anoxic zone is sulfidic [8]. The magnetotaxis behavior is believed to help MTB find the ideal survival environment along the geomagnetic field lines.

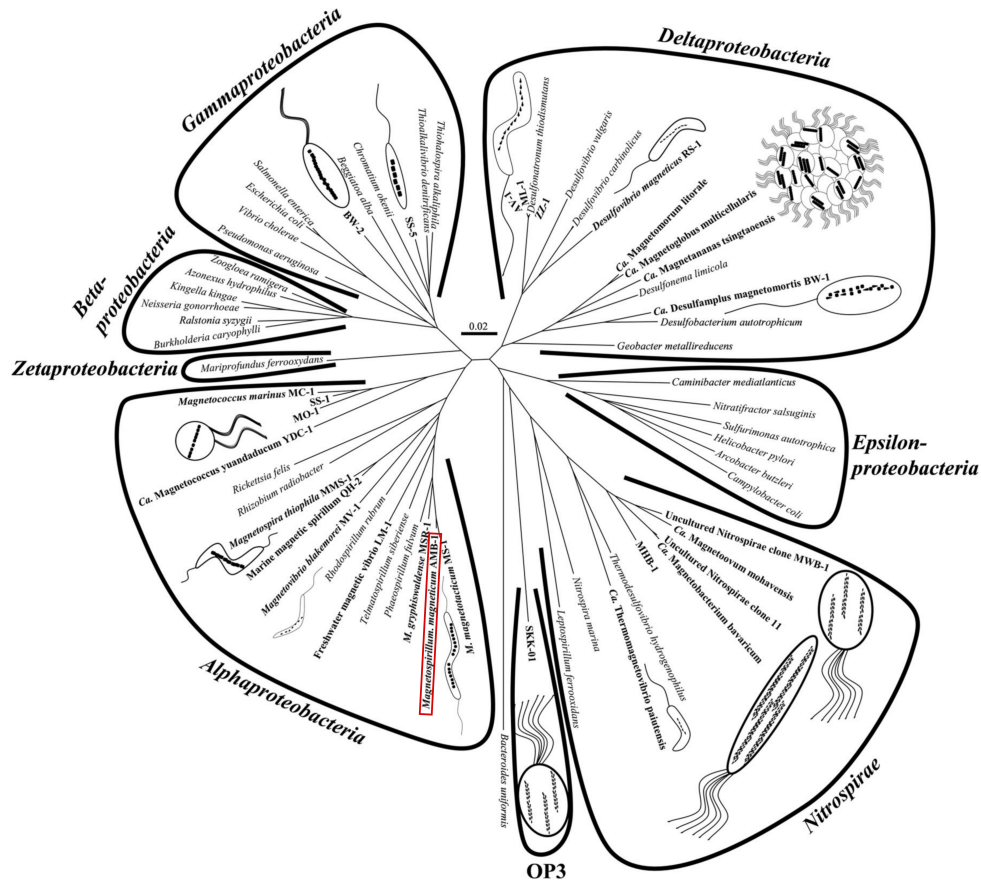


Figure 1.1: Phylogenetic distribution of both cultured and uncultured MTB in the *Alpha*-, *Gamma*-, and *Deltaproteobacteria* classes of the *Proteobacteria* phylum, the *Nitrospirae* phylum and the candidate division OP3. MTB are in bold. The red rectangle indicates strain AMB-1, used in the work presented in this thesis. Reproduced and modified from [5] with permission from the *American Society for Microbiology (ASM)*.

MTB were thought to be growing only in environments with ambient temperature and pH values close to neutral. However, in 2010, Lefèvre et al. discovered MTB in

water and surface sediment samples taken from the Great Boiling Springs (Nevada, USA) with a probable upper survival limit of $\sim 63^{\circ}\text{C}$ [9]. In addition, the same group isolated several strains of MTB from mud and water samples collected from highly alkaline aquatic environments ($\text{pH} \sim 9.5$) [10]. These MTB grew healthily at $\text{pH} 9.0 - 9.5$, but not at $\text{pH} \leq 8$, which demonstrated their requirement for highly alkaline environment.

The great diversity of MTB is obvious since a large number of different morphotypes has been observed in environmental samples. Morphotypes that have been observed include cocci, ovoid, spirilla, bacilli and vibrios. Despite their different morphologies, all MTB studied so far are gram-negative bacteria with one exception: some uncultured, freshwater MTB belonging to the Nitrospirae phylum appear to have a more complex cell wall structure [11, 12]. In addition, until now, all studied MTB are motile by means of flagella, but the arrangement of these flagella differs: polar, bipolar or in tufts [5, 7]. The speciation of MTB is the result of genetic differences and evolutionary relations, and often leads to different morphologies and physiological requirements. Fig. 1.1 presents a portion of the phylogenetic tree of cultured and uncultured MTB. MTB are associated with five major lineages within the domain *Bacteria*: the *Alphaproteobacteria*, *Gammaproteobacteria*, and *Deltaproteobacteria* classes (all belong to the *Proteobacteria* phylum), the *Nitrospirae* phylum and the candidate division OP3, part of the *Planctomycetes-Verrucomicrobia-Chlamydiae* (PVC) bacterial superphylum [13]. Discovery of thermophilic, obligately alkilophilic MTB and low abundance MTB belonging to the candidate OP3 division indicate that the diversity phylogenetic distribution of MTB is likely underestimated [5, 7].

1.1.3 Structural properties - magnetosomes

Magnetosomes, accounting for the magnetotactic lifestyle, are specialized organelles of MTB. Magnetosomes are intracellular structures and each consists of a magnetic inorganic crystal enveloped by an organic membrane. The morphology and composition of crystals varies, but it is considered to be consistent within one bacterial species or strain [14]. As mentioned before, the magnetic crystals are made of either high purity iron oxide, magnetite (Fe_3O_4) or iron sulfide, greigite (Fe_3S_4). At room temperature, both magnetite and greigite minerals have a permanent magnetic moment which can help perform magnetotaxis. It has been reported that a unique type of MTB contain both magnetite and greigite particles [15].

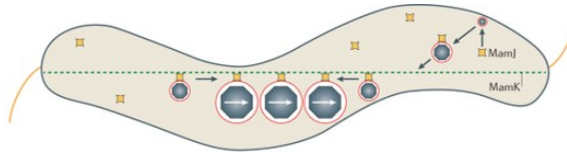


Figure 1.2: Schematic representation of the magnetosome chain assembly in *Magnetospirillum*. The interaction between MamK filaments (green dashed line) and MamJ (yellow star) helps the assembly of magnetosome chain. Reproduced from [16] with permission from *Springer*.

The magnetosome biogenesis process in MTB has been investigated, mainly for the genus *Magnetospirillum*. Genetic studies have shown that all functions specific to this process are associated with about 30 genes [16]. In addition, all of them are clustered in a single chromosomal region called the genomic magnetosome island (MAI) [17, 18]. The magnetosome biogenesis process starts with the formation of the magnetosome membrane, which is an invagination of the cytoplasmic membrane [19, 20, 21]. The process continues with iron accumulating in the vesicles formed by the magnetosome membrane and then nucleation of magnetite crystals. The following step is

magnetosome chain assembly, which is achieved by a cooperation between magnetic interactions and active assembly mechanisms [16]. Active assembly mechanisms are mediated by proteins, and, for strains AMB-1 and MSR-1, the two most important proteins are MamK and MamJ. MamK is an actin-like protein that forms bundles of filaments transversing the cell, and MamJ is a connector attaching magnetosomes to MamK filaments (Fig. 1.2). Last, during cell division, the separation of magnetosome chains occurs, and the magnetosomes are properly segregated and equally inherited by the two daughter cells.

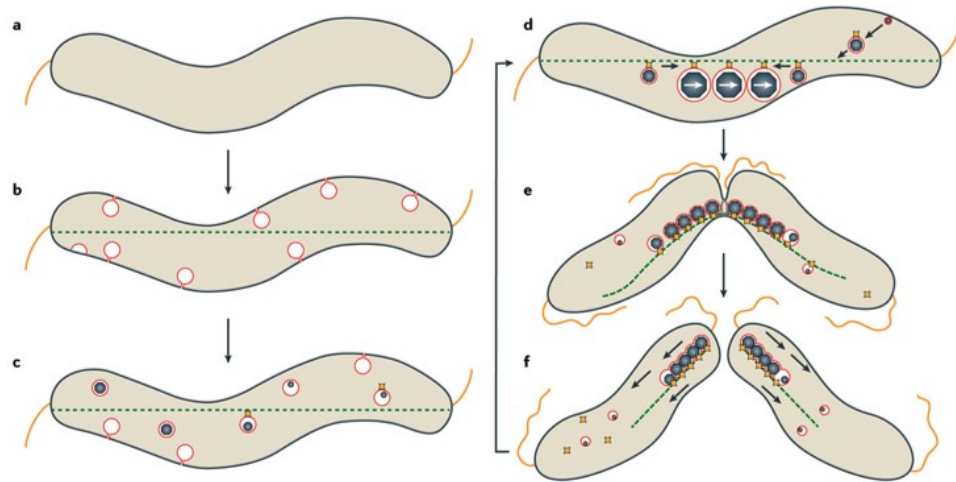


Figure 1.3: Magnetosome biomineralization model for MSR-1. (a) “Empty” cell with no magnetosome. (b) Formation of magnetosome vesicles (red circles) through invagination of the cytoplasmic membrane. (c) Magnetite biomineralization starts in the newly formed vesicles, and the vesicles are attached to the MamK filament through MamK and MamJ interaction. (d) Mature magnetosomes form a chain in the middle of the cell. (e) Cell division is initiated. (f) Repositioning of magnetosome chains after the cell division. Reproduced from [16] with permission from *Springer*.

The whole process of magnetosome biogenesis, including formation of magnetosome membrane, biomineralization, chain formation and cell division in MSR-1 is shown in Fig. 1.3. Other than MamK and MamJ mentioned above, many other

proteins have been identified in the MAI, but the roles of some of them are still under investigation. For example, a possible interaction between MamK and FtsZ is suggested and a truncated FtsZ homologue known as FtsZm is found where cell division happens [22, 23]. However, it is suggested by genetic studies that FtsZm is not required for cell division [24, 25]. With the progress made in understanding MTB genetics, a “magnetized” *Rhodospirillum rubrum* capable of magnetosome biogenesis, formation of magnetosome chain and responding to magnetic field was created, which proves the possibility of reconstructing magnetosomes in non-magnetotactic bacteria and the potential of utilizing magnetosomes in biotechnology [26]. For instance, some of the genes involving the formation of magnetosome chain have been introduced in mammalian cells to enhance mammalian cells’ contrast in MRI [27]. We have helped our collaborator, Donna E. Goldhawk (Western University), with studying the interactions between two proteins in the MAI domain, MamI and MamL, when expressed in mammalian cells. The interaction was confirmed by confocal fluorescence microscopy and fluorescence correlation spectroscopy (FCS). MamI and MamL were found co-localized in an intracellular compartment. These results support that MamI and MamL expressed in mammalian cells have a potential role of initiating formation of a rudimentary magnetosome-like nanoparticle. The work done for the FCS data analysis is not included in this thesis.

1.1.4 Applications of magnetotactic bacteria

MTB have potential applications in different fields ranging from biomedical and biotechnological applications to wastewater treatment and geology [28, 29].

One popular direction is microrobotics. Martel and his coworkers showed that

MTB could push micro-size beads along preplanned paths by controlling the external magnetic field [30]. They attached *Magnetospirillum gryphiswaldense* bacteria to 3 μm beads made of melamine-formaldehyde resin which was hydrophilic, and the measured average speed of beads pushed by single bacterium was 7.5 $\mu\text{m/s}$. In addition, they mentioned that the direction of the movement was controlled by permanent magnets or a simple program in C++, but they did not show details. One example of clinical application is isolation of pathogens. Chen coated the surface of MO-1 cells with rabbit anti-MO-1 cell polyclonal antibodies, and then attached the microrobots to *Staphylococcus aureus* [31]. They reported that they have successfully attached the modified MO-1 cells to *S. aureus* and the highest attachment percentage achieved was 30% in 30 minutes. Chen's work shows the potential of MTB in separation of pathogens, diagnosis of diseases.

Magnetic resonance imaging (MRI) contrast-agent is another promising application for MTB. Magnetic nanoparticles can enhance MRI signal, which helps distinguish diseased tissue from normal tissue. Benoit showed that MTB could target tumors in mice and, when using MRI, provided positive contrast for visualization [32]. Interestingly, the ability of AMB-1 cells to generate positive contrast depended on Fe-source in cell culture medium. Their study provided a proof that bacterial magnetite could improve positive MRI contrast *in vivo*. The authors mentioned that if genes responsible for magnetosome production are expressed in mammalian cells, MRI monitoring of cell-based therapies could be improved [32]. Goldhawk et al. took a first step in that direction by introducing a putative iron transporter gene, MagA, in mammalian cells [27].

1.1.5 *Magnetospirillum magneticum* AMB-1

AMB-1 is the MTB strain used in all the experiments presented in this thesis and it is one of the most studied strains. *Magnetospirillum magneticum*, AMB-1, was first reported, isolated and cultured in a pure culture from freshwater sediments from a natural spring in Tokyo by Matsunaga [33]. This stain is microaerophilic with a helical shape and one flagellum at each pole (Fig. 1.4). The average cell length is 3 – 4 μm and average cell width is 0.4 – 0.6 μm [33, 34, 35]. AMB-1 cells produce cuboctahedral magnetite (Fe_3O_4) crystals, with an average diameter per crystal of 50 nm [16, 33]. These crystals are assembled into a magnetosome chain along the long axis of the cell, and the chain is often fragmented into 3 to 5 subchains, as shown in Fig. 1.4 [36].

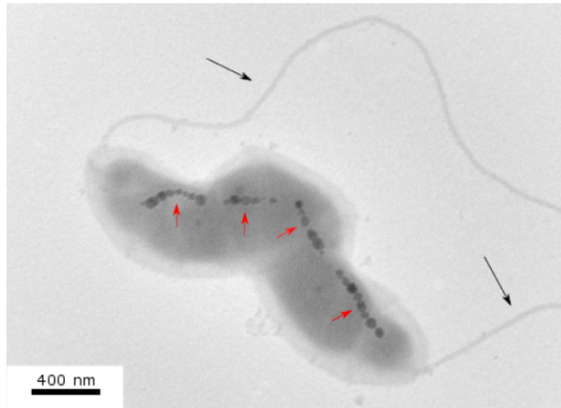


Figure 1.4: TEM observation of an AMB-1 cell. Magnetosome subchains are indicated by red arrows. Black arrows indicate the two flagella. Reproduced from [37] with permission from *JoVE*.

The average swimming speed of AMB-1 cells is reported to be 44 – 49 $\mu\text{m}/\text{s}$, independent of cell length or external magnetic field value [34, 35]. Magnetic moment has been measured by different methods, and the average value falls in the range of

$0.5 - 10 \times 10^{-16}$ A·m²/cell, increasing with cell length [35, 38, 39, 40, 41]. From cell rotational trajectories, Le Nagard found, for AMB-1 cells, that there was a misalignment between the cell magnetic moment and the cell long axis, which had an average value of 6° and could be as high as 20° [41].

1.2 Motion of MTB

The swimming behavior of bacteria involves rotations of both the cell body and the flagella, and my work revolved around a better understanding of the drag forces on bacteria when they are swimming.

1.2.1 Life at low Reynolds number

To understand how MTB, micro-size swimmers, move, we need to solve the motion of the surrounding fluid first [42, 43]. The motion of an incompressible Newtonian fluid with a constant density ρ and a constant kinematic viscosity ν is determined by the Navier-Stokes equations:

$$\frac{\partial \vec{u}}{\partial t} + \vec{u} \cdot \nabla \vec{u} = -\frac{1}{\rho} \nabla p + \nu \nabla^2 \vec{u}, \quad (1.2.1)$$

$$\nabla \cdot \vec{u} = 0. \quad (1.2.2)$$

The fluid in the region exterior to the organism with velocity field $\vec{u} = (u(\vec{r}, t), v(\vec{r}, t), w(\vec{r}, t))$ and pressure field $p(\vec{r}, t)$, where $\vec{r} = (x, y, z)$, should satisfy both Eqs. 1.2.1 and 1.2.2.

To rewrite Eqs. 1.2.1 and 1.2.2 in terms of dimensionless variables, L , T and U

are defined to be the characteristic length, time and speed of the swimming motion, respectively. Dimensionless variables are obtained by:

$$\tilde{u} = \frac{\vec{u}}{U}, \quad \tilde{r} = \frac{\vec{r}}{L}, \quad \tilde{t} = \frac{t}{T}, \quad \tilde{p} = \frac{pL}{\nu\rho U}. \quad (1.2.3)$$

The Navier-Stokes equations Eq. 1.2.1 and Eq. 1.2.2 then become:

$$\frac{\partial \tilde{u}}{\partial \tilde{t}} + \tilde{u} \cdot \tilde{\nabla} \tilde{u} = -\frac{\nu}{UL} \tilde{\nabla} \tilde{p} + \frac{\nu}{UL} \tilde{\nabla}^2 \tilde{u}, \quad (1.2.4)$$

$$\tilde{\nabla} \cdot \tilde{u} = 0. \quad (1.2.5)$$

The Reynolds number Re is defined as:

$$Re = \frac{UL}{\nu} = \frac{\rho UL}{\eta}, \quad (1.2.6)$$

where η is the dynamic viscosity of the fluid ($\eta = \rho\nu$). Then, Eqs. 1.2.4 and 1.2.5 become:

$$Re \left(\frac{\partial \tilde{u}}{\partial \tilde{t}} + \tilde{u} \cdot \tilde{\nabla} \tilde{u} \right) = -\tilde{\nabla} \tilde{p} + \tilde{\nabla}^2 \tilde{u}, \quad (1.2.7)$$

$$\tilde{\nabla} \cdot \tilde{u} = 0. \quad (1.2.8)$$

These equations are still Navier-Stokes equations but with variables (\tilde{u} , \tilde{p} and \tilde{t}) on the order of ~ 1 for the considered process.

In water ($\rho \approx 10^3 \text{ kg/m}^3$, $\eta \approx 10^{-3} \text{ Pa}\cdot\text{s}$), consider an AMB-1 cell with $L \approx 3 - 4 \text{ }\mu\text{m}$ and $U \approx 40 - 50 \text{ }\mu\text{m/s}$, a Reynolds number $Re \approx 10^{-4}$ is obtained. A ciliated protozoan has $L \approx 100 \text{ }\mu\text{m}$ and $U \approx 1 \text{ mm/s}$, and therefore $Re \approx 0.1$ [44].

A medium sized fish with $L \approx 50$ cm and $U \approx 100$ cm/s gives a Reynolds number $Re \approx 5 \times 10^5$. By comparing these values of Re , it is obvious that MTB are micro-size swimmers living in a low Reynolds number world. Thus, the limit of $Re \rightarrow 0$ is studied and Eqs. 1.2.7 and 1.2.8 simplify to the Stokes equations (where the superscript \sim was dropped for simplicity):

$$-\nabla p + \nabla^2 \vec{u} = 0, \quad (1.2.9)$$

$$\nabla \cdot \vec{u} = 0. \quad (1.2.10)$$

Physically, Re is dimensionless and it is the ratio of the inertial forces to the viscous forces [42]. For organisms with $Re \ll 1$, it means that the frictional drag generated by the surrounding fluid is much greater than their inertia. Let us consider the swimming motion of one MTB cell with mass m , radius r , length l and speed v in water. Suppose the cell suddenly stop its motors, then the only force left acting on the cell body is the drag force, which is simply $F_{drag} = f_d v$ at low Reynolds number, where f_d is the drag coefficient, which relates to the surrounding fluid's viscosity η and the object's size and shape (see section 1.2.4). Thus, we have:

$$m \frac{dv}{dt} + f_d v = 0, \quad (1.2.11)$$

after integration:

$$v(t) = v(0) e^{-\frac{f_d}{m} t}. \quad (1.2.12)$$

The distance that the cell coasts due to the inertia is

$$x = \int_0^{\infty} v(t)dt = \int_0^{\infty} v(0)e^{-\frac{f_d}{m}t}dt = -v(0)\frac{m}{f_d}e^{-\frac{f_d}{m}t}\Big|_0^{\infty} = v(0)\frac{m}{f_d}. \quad (1.2.13)$$

The density of bacteria is comparable to water, thus, $\rho_b \approx 10^3 \text{ kg/m}^3$. Assume our cell is a sphere of $r \approx 2 \text{ }\mu\text{m}$ with initial swimming speed $v = 45\mu\text{m/s}$, and f_d for sphere is $f_d = 6\pi\eta r$. Thus, we have $m = \frac{4}{3}\pi r^3 \rho_b \approx 3 \times 10^{-14} \text{ kg}$ and $f_d \approx 3.8 \times 10^{-8} \text{ N}\cdot\text{s/m} = 38 \text{ nN}\cdot\text{s/m}$. Then the coasting distance is $x \approx 3.6 \times 10^{-11} \text{ m} = 36 \text{ pm} = 0.36 \text{ \AA}$, which is less than the diameter of a water molecule [45]. This suggests that the bacterium stops instantaneously after the motors stop, which indicates that the viscous response of the surrounding fluid is instantaneous [44]. As a result, a cell swimming at low Re is force- and torque-free:

$$\sum_i \vec{F} = \vec{F}_{fluid} + \vec{F}_{ext} = \vec{0}, \quad (1.2.14)$$

$$\sum_i \vec{L} = \vec{L}_{fluid} + \vec{L}_{ext} = \vec{0}, \quad (1.2.15)$$

where \vec{F}_{ext} and \vec{L}_{ext} are the net external force and torque acting on the cell. For example, the external force could be applied by an optical trap, and the external torque could be a magnetic torque [46].

1.2.2 Swimming behavior - propulsive forces

Bacteria swim by moving their flagella whose main component is thin filaments with a length of a few micrometers and a width of about 20 nm [47]. The filament was thought to propagate a helical wave but it turned out otherwise. The bacterial

flagellum is actually a propeller, and the filament rotates rigidly to push or pull bacteria [48]. Each flagellum has three main parts: the hook, the helical filament and a set of rings embedded in the cell wall and cytoplasmic membrane (basal body) (Fig. 1.5) [49]. The basal body contains the rotary motor, which is made of stator and rotor part. The stator units are anchored to the cell wall and form transmembrane channels. The rotation of the rotor units is powered by a proton or sodium ion flow through these channels.

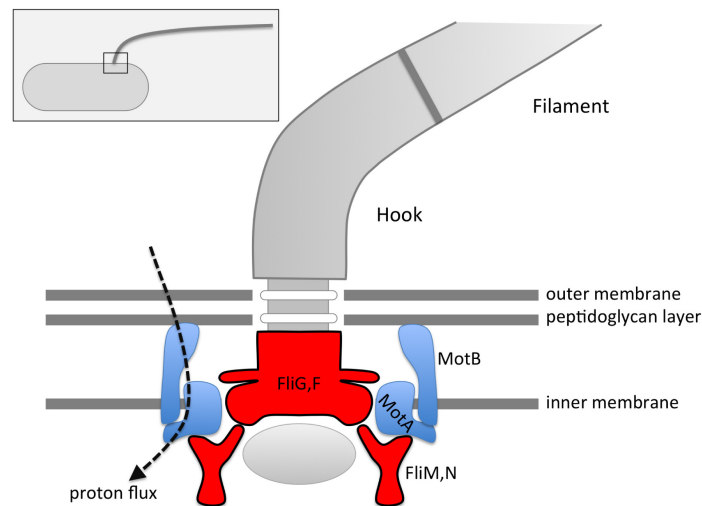


Figure 1.5: Structure of the Gram-negative bacterial flagellum: The stator and rotor consist of proteins in blue and red, respectively. A proton flow through the stator drives the rotation of the central rotor. The flagellar hook and filament then move with the rotor. The structure is simplified and not all proteins are included. Reproduced from [47] with permission from *Elsevier*.

As mentioned in section 1.1.5, AMB-1 cells have one flagellum at each pole. Murat et al. studied how these two polar flagella are coordinated during different types of motion by imaging cells with fluorescently labeled flagella [50]. They showed that the counterclockwise rotation of the lagging flagellum propels the cells. They also analyzed cell body motion during cell movement by following a fluorescently labeled,

fixed protein in the cell. Following the fluorescent tracks of the protein, they found that the AMB-1 cell rotates in the clockwise direction during movement [50]. Thus, when swimming, the lagging flagella and cell body rotate in opposite directions (Fig. 1.6). A swimming cell at low Re is force- and torque-free (section 1.2.1), and when consider this in the reference frame of the cell body, the rotation of the cell body in the direction opposite to that of the lagging flagella is to balance the torque generated by the rotation of the flagella. The rotation of the flagella is at the origin of the propulsive force that pushes the cell forward. Observing similar maximum speed of AMB-1 when performing north- and southbound runs, the authors suggested that the two flagella can generate similar levels of torque [50].

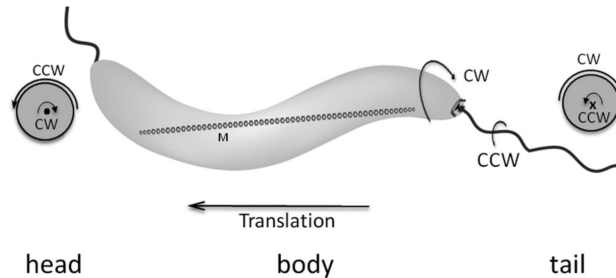


Figure 1.6: Schematic representation of an AMB-1 cell showing translation and cell body and flagellar rotation directions. • and × show views from the head and tail ends, respectively. Reproduced from [50] with permission from *American Society for Microbiology*.

1.2.3 Thermal forces and diffusion

All sufficiently small particles in suspension are subject to forces due to collisions with water and other molecules in the surrounding fluid [45]. The amplitude of these collisional forces are proportional to the temperature of the fluid molecules, thus, they are called thermal forces. The object is said to have thermal energy. The resulting

thermal motion frequently changes direction because of the randomly directed thermal forces, and this motion is called diffusion.

MTB are microswimmers, thus, they perform diffusive motion in addition to their self-propulsion. Considering translational diffusion first, if a particle is released at x_0 and allowed to diffuse in one dimension (x here, same for y and z), then the probability of finding it at position x at a later time $t > 0$ is:

$$p(x, t) = \frac{1}{\sqrt{4\pi D_x t}} e^{-\frac{(x-x_0)^2}{4D_x t}}, \quad (1.2.16)$$

where D_x is the translational diffusion coefficient in the x - direction. This probability distribution is illustrated in Fig. 1.7. It is a Gaussian distribution with variance $\sigma^2 = 2D_x t$. The mean-squared-displacement (MSD), $\langle (x(t) - x_0)^2 \rangle$, which is equal to the variance, increases linearly with time (Fig. 1.8).

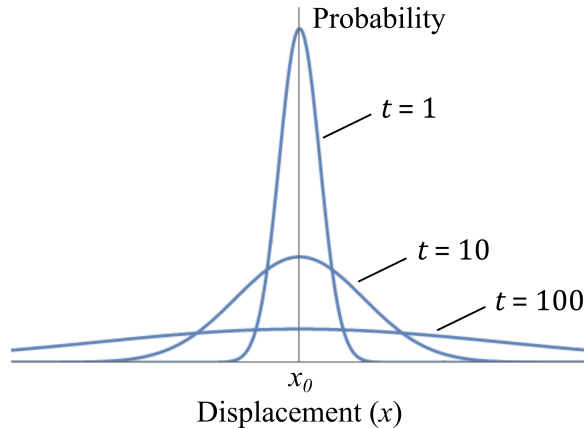


Figure 1.7: Diffusion of a particle released at x_0 at time 0. Curves show the probability of finding a particle at position x with increasing times.

In addition to translational diffusion, microswimmers undergo rotational diffusion. Rotational diffusion changes the orientation of the particle, and similar to translational diffusion, the probability distribution for rotation around a single axis is a

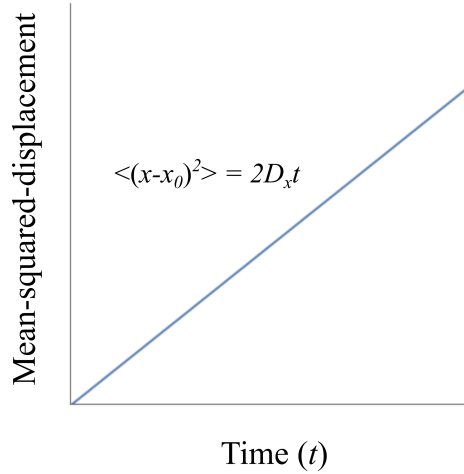


Figure 1.8: Mean-squared-displacement of a particle released at x_0 at time 0 under diffusion increases linearly with time.

Gaussian distribution:

$$p(\phi, t) = \frac{1}{\sqrt{4\pi D_\phi t}} e^{-\frac{(\phi - \phi_0)^2}{4D_\phi t}}, \quad (1.2.17)$$

with the rotational diffusion coefficient in the ϕ - direction D_ϕ . Thus, the mean-squared angular deviation from the initial orientation ϕ_0 increases also linearly with time

$$\langle (\phi(t) - \phi_0)^2 \rangle = 2D_\phi t. \quad (1.2.18)$$

1.2.4 Drag coefficients

A drag coefficient quantifies the resistance or drag of an object in a fluid environment. The relationship between the diffusion coefficient and the drag coefficient is given by Stokes-Einstein relation:

$$D = \frac{kT}{f}, \quad (1.2.19)$$

where k is the Boltzmann constant, T is the absolute temperature, D is the diffusion coefficient and f is the drag coefficient. Stokes-Einstein relation provides a link between the microscopic and macroscopic theories of diffusion by relating a molecular parameter, the drag coefficient, to a macroscopic parameter, the diffusion coefficient [45]. As mentioned, the drag coefficient depends on the size and shape of the object and the viscosity of the surrounding fluid, and formulas for the four principal drag coefficients of several common shape objects are shown in Table 1.1. For translational drags, the drag force is $\vec{F}_{fluid} = f_t \vec{v}$, where \vec{v} is the velocity. Similarly, for rotational drags, the drag torque is $\vec{L}_{fluid} = f_r \vec{\omega}$, where $\vec{\omega}$ is the angular velocity.

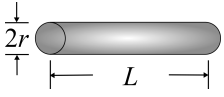
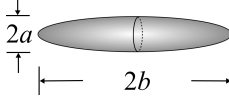


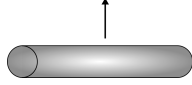
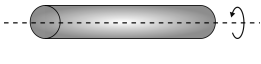
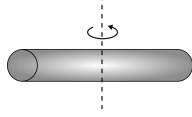
Parameter	Direction	Cylinder ($L \gg r$)	Ellipsoid ($b \gg a$)	Sphere
				
$f_{t_{\parallel}}$		$\frac{2\pi\eta L}{\ln(L/2r)-0.2}$	$\frac{2\pi\eta(2b)}{\ln(2b/a)-0.5}$	$6\pi\eta r$
$f_{t_{\perp}}$		$\frac{4\pi\eta L}{\ln(L/2r)+0.84}$	$\frac{4\pi\eta(2b)}{\ln(2b/a)+0.5}$	$6\pi\eta r$
$f_{r_{\parallel}}$		$\frac{\frac{1}{3}\pi\eta L^3}{\ln(L/2r)-0.66}$	$\frac{\frac{1}{3}\pi\eta(2b)^3}{\ln(2b/a)-0.5}$	$8\pi\eta r^3$
$f_{r_{\perp}}$		$4\pi\eta r^2 L$	$\frac{8}{3}\pi\eta a^2(2b)$	$8\pi\eta r^3$

Table 1.1: Drag coefficients of objects with different shapes. The expressions are from reference [45]. Expressions for sphere are exact drag coefficients and for cylinder and ellipsoid are approximations.

Drag coefficients of microswimmers are often used to measure other things. They

can be used to estimate the torque of the flagellar motor of different kinds of bacteria, such as *Streptococcus* and *E. coli* [51, 52, 53]. For MTB, the so-called "U-turn" method is often employed to measure the magnetic moment of individual cells, and f_r value is especially important as accurate measurement of μ can only be made if the value of f_r is precisely known.

1.2.5 Interaction with a magnetic field

As mentioned in section 1.1.3, magnetosomes contain magnetite (Fe_3O_4) or greigite (Fe_3S_4) crystals, and the magnetosome chain functions as a single magnetic dipole with a magnetic moment $\vec{\mu}$. The orientation of the magnetic moment is fixed with respect to the cell body, thus, its passive alignment with magnetic field \vec{B} results in controlled orientation of cell body and swimming direction. The magnetic energy of the system is:

$$E_m = -\vec{\mu} \cdot \vec{B} = -\mu B \cos \alpha, \quad (1.2.20)$$

where α is the angle between the magnetic field \vec{B} and the magnetic moment $\vec{\mu}$ (Fig. 1.9). The expectation value of $\cos \alpha$ indicating the normalized projection of the magnetic moment onto the direction of the magnetic field can be used to characterize the alignment with a magnetic field [47]. According to Boltzmann's law, in thermal equilibrium, the probability of α is given by:

$$p(\alpha, \varphi) = \frac{1}{Z} e^{-\frac{E_m}{kT}}, \text{ with } Z = \text{constant} = \int e^{-\frac{E_m}{kT}} dV, \quad (1.2.21)$$

where Z is the partition function obtained by integrating $e^{-\frac{E_m}{kT}}$ over all possible (α, φ) .

Then,

$$\langle \cos \alpha \rangle = \frac{\int \cos \alpha e^{-\frac{E_m}{kT}} dV}{\int e^{-\frac{E_m}{kT}} dV} = L\left(\frac{\mu B}{kT}\right), \quad (1.2.22)$$

where $L(x) = \coth(x) - \frac{1}{x}$ is the Langevin function (Fig. 1.9). For a MTB cell with typical magnetic moment $\mu = 10^{-15}$ A·m² in the earth magnetic field $B \approx 0.5$ G at room temperature $T = 300$ K, this model leads to $\langle \cos \alpha \rangle \approx 0.9$. From this calculation, Frankel concluded that the magnetic moments of MTB cells were sufficient for them to swim along geomagnetic field lines and that magnetotaxis was an efficient process [54].

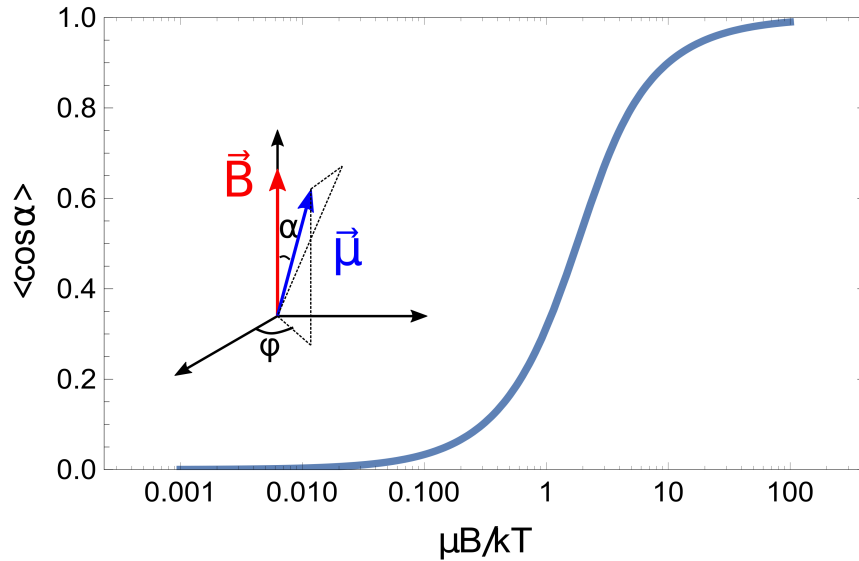


Figure 1.9: MTB change orientation due to the alignment of their magnetic moment $\vec{\mu}$ and magnetic field \vec{B} . The degree of alignment is quantified by the cosine of the angle α , the angle between the magnetic moment and the magnetic field. φ is the angle denoting the orientation of the projection of $\vec{\mu}$ in the plane perpendicular to \vec{B} . Depending on the ratio of magnetic to thermal energy, the degree of alignment is given by the Langevin function (blue curve).

A homogeneous magnetic field only exerts a torque on a magnetic moment. Thus,

a homogeneous magnetic field changes the orientation of MTB cells, but does not pull them. The torque is given by:

$$\vec{L}_{magnetic} = \vec{\mu} \times \vec{B}. \quad (1.2.23)$$

The viscous drag torque applied by the fluid on the cell is $\vec{L}_{fluid} = f_r \frac{d\vec{\alpha}}{dt}$, where f_r is the rotational drag coefficient. Because of a zero net torque (small Reynolds number), the rotational drag must on average exactly balance the torque exerted by magnetic field:

$$\vec{L}_{magnetic} + \vec{L}_{fluid} = \vec{\mu} \times \vec{B} + f_r \frac{d\vec{\alpha}}{dt} = \vec{0}. \quad (1.2.24)$$

Therefore, μ can be measured from rotational trajectories if B and f_r are known.

Chapter 2

Methods

2.1 Simulations of rotational diffusion

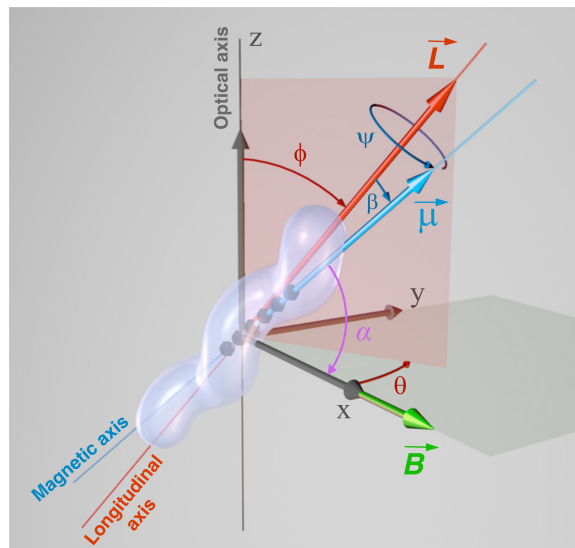


Figure 2.1: Orientation of the cell with respect to the focal plane and the external magnetic field. Here, the gray plane is the focal plane and the red plane is the $\vec{L} - z$ plane. \vec{L} , $\vec{\mu}$ and \vec{B} represent the cell longitudinal axis, the cell magnetic moment and magnetic field, respectively.

A magnetic cell undergoing rotational diffusion in a uniform magnetic field was simulated using Mathematica (Wolfram Research). The cell was assimilated to an elongated rigid body with rotational symmetry around its longitudinal axis (\vec{L}), with rotational drag coefficients, $f_{r_{\perp}}$ and $f_{r_{\parallel}}$, related to the rotations perpendicular or parallel to \vec{L} . The position of \vec{L} is determined by the polar angle ϕ and the azimuthal angle θ (Fig. 2.1). The angle between the magnetic moment $\vec{\mu}$ and magnetic field \vec{B} is α as in section 1.2.5. There is a constant misalignment (section 1.1.5) between the cell's magnetic moment $\vec{\mu}$ and \vec{L} , denoted as β . The orientation of $\vec{\mu}$ with respect to \vec{L} is indicated by the constant angle β and by the rotation ψ around \vec{L} . By performing a series of four small rotations, the cell's orientation was updated every $\delta t = 1$ ms. The cell was first allowed to go through diffusion around its three principal axes of rotation, in the order of $\vec{L} \times \vec{z}$, $\vec{L} \times (\vec{L} \times \vec{z})$ and \vec{L} . These three rotations changed the angle ϕ , θ and ψ , respectively. For these three rotations, angular displacements were drawn from Gaussian distributions (Eq. 1.2.17) with variance $2D_{r_{\perp}}\delta t$, $2D_{r_{\perp}}\delta t$, and $2D_{r_{\parallel}}\delta t$ (section 1.2.3), where $D_{r_{\perp}} = kT/f_{r_{\perp}}$ (Eq. 1.2.19) is the rotational diffusion coefficient perpendicular to the cell longitudinal axis (transversal rotational diffusion coefficient) and $D_{r_{\parallel}} = kT/f_{r_{\parallel}}$ is the rotational diffusion coefficient of rotation around the cell longitudinal axis (longitudinal rotational diffusion coefficient). In the presence of an external magnetic field, \vec{B} , an additional rotation was performed, due to the magnetic torque. The whole cell (both \vec{L} and $\vec{\mu}$) was rotated around $\vec{\mu} \times \vec{B}$ by an angle $d\alpha = |\vec{\mu} \times \vec{B}|\delta t/f_{r_{\perp}}$ (Eq. 1.2.24). The (x, y, z) coordinates of \vec{L} and $\vec{\mu}$ were saved at each step. Then the experimental accessible variables, θ and ϕ , were calculated from \vec{L} and $\vec{\mu}$. The apparent orientation of the cell on the focal plane, θ , was obtained by projecting \vec{L} onto the $x - y$ plane. The cell's apparent rotation

around its longitudinal axis, ψ , was calculated as the angle between the $\vec{L} - z$ plane (red plane in Fig. 2.1) and the vector $\vec{\mu} - (\vec{\mu} \cdot \vec{L}/L^2)\vec{L}$ ($(\vec{\mu} \cdot \vec{L}/L^2)\vec{L}$ is a vector with same length as $\vec{\mu}$ in the \vec{L} direction). Simulations were typically run for 2000 steps (2 s) with physical parameters measured for AMB-1 cells: $D_{r_{\perp}} = 0.28 \text{ s}^{-1}$, $D_{r_{\parallel}} = 0.01 \text{ s}^{-1}$ and $\mu = 0.42 \times 10^{-15} \text{ A}\cdot\text{m}^2$.

2.2 Cell culture

2.2.1 Growth medium

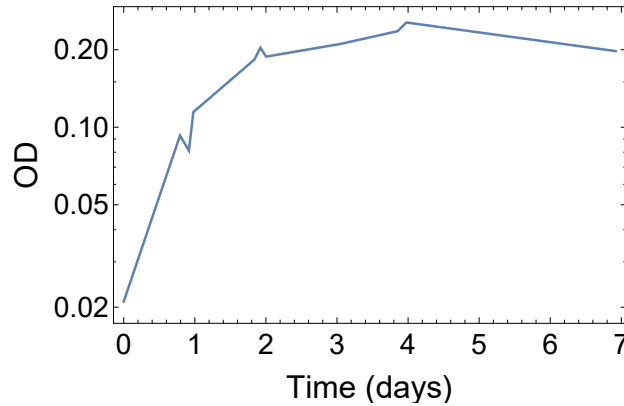


Figure 2.2: Growth curve of a culture. y - axis is the measured optical density.

Cells of *M. magneticum* strain AMB-1 (obtained from ATCC, 700264) were grown under iron-rich condition following the protocol in Ref. [37]. Cells were grown at 30°C in 60 mL of growth medium inside 125 mL sealed glass bottle. 1 L of the liquid medium contains 1 mL trace mineral supplement solution, 0.1 g KH_2PO_4 , 0.15 g $\text{MgSO}_4 \cdot 7\text{H}_2\text{O}$, 2.38 g HEPES, 0.34 g NaNO_3 , 0.1 g yeast extract, 3 g soy bean peptone (BD Bacto Soytone), 4.35 mL potassium lactate and 5 mL 10 nM Fe(III) citrate (with pH adjusted to 7.0 with NaOH). O_2 in the headspace of the bottle or dissolved in

the medium was removed by bubbling N_2 in the headspace or in the solution. The medium was then autoclaved to ensure sterility. Right before inoculation, 1 mL of O_2 was added to the headspace (65 mL) to reach a 1.5% O_2 microaerobic environment ideal for AMB-1 growth. Then, 1 mL of a 3 to 7 days old AMB-1 cell culture was inoculated into the fresh medium.

Fig. 2.2 is an example growth curve for an AMB-1 culture. The bacteria would follow an exponential growth at first:

$$N = N_0 \times 2^n, \quad (2.2.1)$$

where N_0 is the number of bacteria at the beginning of the time interval (optical density is proportional to cell number), N is the number of bacteria at the end of the time interval and n is the number of generations. Consider two points from Fig. 2.2 during the exponential growth phase, $(0, 0.008)$ and $(19/24, 0.05)$, and then we had $0.05 = 0.008 \times 2^n$, thus, $n = 2.6$. Therefore, in 19 hours (19/24 day), we had 2.6 generations of bacteria. The cell division time was $19/2.6 \approx 7.2$ hours.

2.2.2 The racetrack method

The iron-rich environment is ideal for the growth of bacteria, providing all kinds of nutrients, thus, some mutants or other bacteria introduced accidentally during inoculation can also survive in the growth medium, causing contamination. The racetrack method was first described by Wolfe to isolate MTB from environmental samples [55].

To perform this method, a glass pipette was first cut leaving the middle part of the pipette (the whole pipette was too long for this experiment). Then, its thinner

end was sealed by melting the glass in the flame of a Bunsen burner. The thinner end was later used to collect magnetotactic bacteria. A small piece of sterile cotton was placed at the neck of the pipette acting as a filter (Fig. 2.3). Using a needle, fresh medium was injected into the thinner part up to the cotton. MTB culture was added to the open end of the pipette. The pipette was kept horizontal and the north pole of a magnetic bar was placed at the sealed end (Fig. 2.3). With the magnetic field, motile MTB can go through the cotton and accumulate at the sealed end of the pipette. After 30 mins, the tip of the pipette was broken and the liquid in the broken tip was transferred into fresh medium using a sterile syringe.

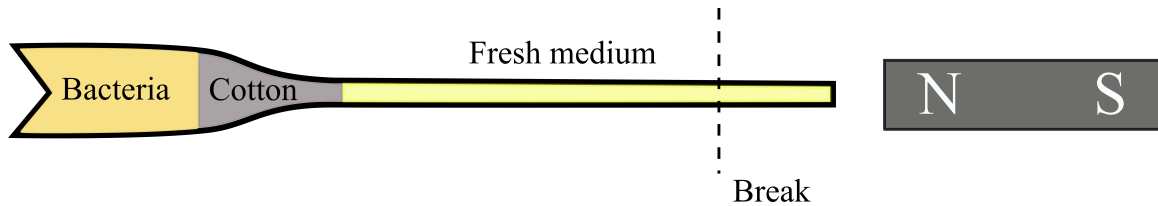


Figure 2.3: Illustration of the racetrack method. Because of the external magnetic field, cells swim towards the sealed end of the pipette. Cells are harvested after 30 mins and then transferred into a bottle of fresh growth medium.

2.2.3 Increasing cell length

Most observed AMB-1 cells have cell length in the range of $L = 2 - 4 \mu\text{m}$. In order to obtain statistics for longer AMB-1 cells, we added to the growth medium $10 \mu\text{g/mL}$ of cephalexin (Sigma-Aldrich), an antibiotic which can block cell division [56, 57]. The time point for addition of cephalexin was two days after inoculation, when bacteria were at the end of the exponential growth phase (Fig. 2.2). To quantify this increase, we examined the cell length distributions of the cephalexin-treated culture and of a control culture four days after inoculation (two days after the addition of cephalexin).

The cell length distributions shown in Fig. 2.4 indicates that cephalixin is indeed blocking cell division as the distribution extends to the right (longer) and cell average length increases (2.8 μm (for the control) vs. 3.2 μm (for the cephalixin-treated culture)). Maki et al. added 60 $\mu\text{g}/\text{mL}$ cephalixin to *E. coli* culture two days after inoculation [58]. Observing the cells 3 to 3.5 hours after the addition of cephalixin, the authors found that the cell average length increased from $\bar{L} = 1.5 \mu\text{m}$ to $\bar{L} = 7.5 \mu\text{m}$. The higher drug concentration and the shorter cell division time for *E. coli* may cause the more significant increase of *E. coli* cell length.

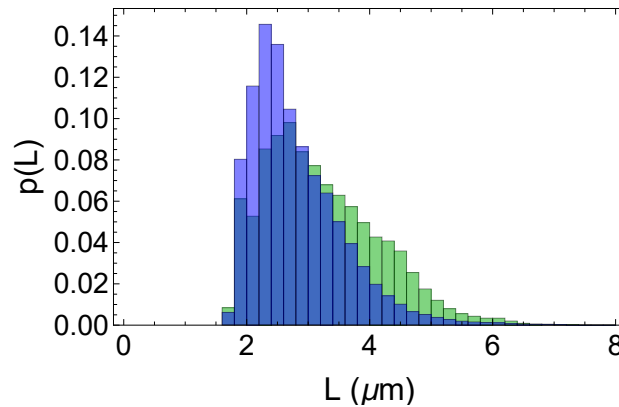


Figure 2.4: Cell length distributions of a control culture (blue) and cephalixin-treated culture (green) of AMB-1 cells.

2.3 Movie acquisition

Experiments were performed using a Nikon Eclipse E200-LED upright microscope with modified stage with a pair of custom-made Helmholtz coils (Fig. 2.5) [41]. A controllable uniform magnetic field up to 1.7 mT was applied parallel to the focal plane by circulating current through the coils, using an Agilent 33120A power supply connected to an Agilent 33502A amplifier.

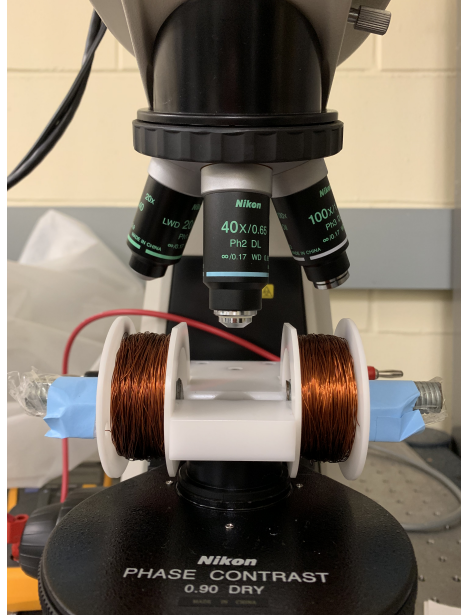


Figure 2.5: Experimental setup of a phase-contrast microscope with modified stage with coils.

Cells were harvested 3 to 5 days after inoculation and killed by heating at 60°C for 15 mins. After cooling down to room temperature, the bacteria suspension was diluted 50 times in fresh medium to achieve an ideal concentration for single cell observation. The diluted solution was then injected into a home-built sample chamber made of a glass slide and a coverslip separated by two melted parafilm strips (Fig. 2.6). The chamber was sealed by vacuum grease or transparent nail polish to avoid evaporation and flow. Movies of cells undergoing translational and rotational diffusion were then immediately recorded at 100 frames per second with a fast CCD camera (AVT Prosilica GE), using the Streampix 5 software. Cells were observed with either a $40\times$ (0.65 NA) or a $100\times$ (1.25 NA) phase-contrast objective. The average movie duration was 17 s, with a minimum length of 4 s.

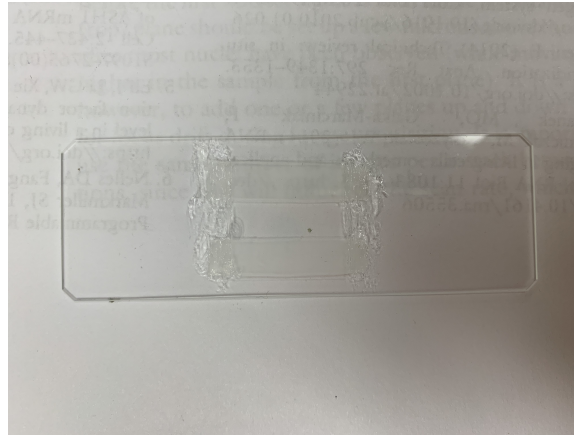


Figure 2.6: Home-built observation chamber made with a glass slide, a coverslip and two parafilm strips and sealed with vacuum grease.

2.4 Cell tracking

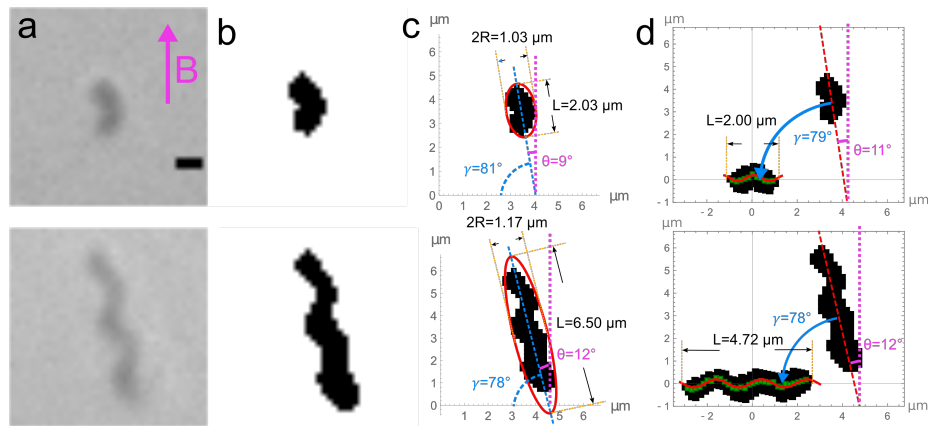


Figure 2.7: Illustration of the image analysis process for a short cell (top row) and a long cell (bottom row). (a) Phase microscopy images of the cells (scalar bar: $1 \mu\text{m}$). (b) Binarized images. (c) Results of elliptical fits. (d) Results of sine fits after rotation of the cells.

Cells were tracked using an algorithm developed by me, and the procedure was illustrated in Fig. 2.7. Images of individual cells were first binarized using ImageJ (Fig. 2.7b), after which the cell was represented by a cloud of points in each frame

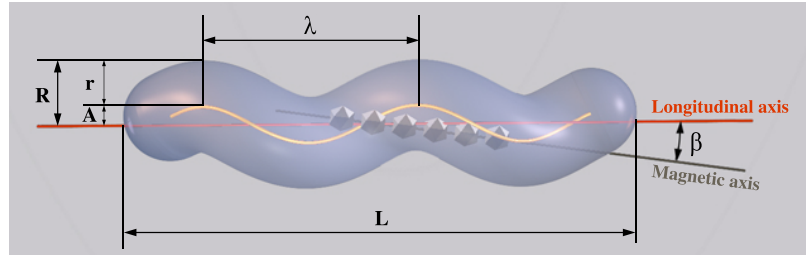


Figure 2.8: Three-dimensional model of a *M. magneticum* cell. The helical backbone, longitudinal axis (which is also the propulsion axis) and magnetic axis (assumed to be exactly aligned with the magnetosome chain) are represented by yellow, red and brown lines, respectively. The different parameters used to characterize the cell geometry and dimensions (L , λ , A , r , R and β) are indicated.

of the movie [59]. The position of the cell was tracked by finding the center of mass of this cloud of points. The apparent orientation of the cell was determined in two different ways using a code written in Mathematica. First, the cell was fit with an ellipse to obtain an estimate of the cell apparent orientation, θ , its length, L , and diameter, R (Fig. 2.7c). The elliptical fit is fast and robust, but it may not capture the exact orientation of helical AMB-1 cells properly. Thus, a more refined fit was then performed to take into account the sinusoidal shape of the projection of the cell body in the focal plane, as first described in Ref. [41] and as illustrated in Fig. 2.7d. The cell was first quickly fit with a line to obtain its approximate orientation. Next, the cell was rotated according to the results of the linear fit to make it approximately horizontal, and such that a sine fit could then be performed. Points were binned vertically to obtain a new series of points considered as the cell backbone, which was then fit with the sine function $A \sin(2\pi x/\lambda + \psi)$, returning parameters including the amplitude (A) and wavelength (λ) of the cell helical backbone, as well as a phase (ψ) giving a direct representation of the rotation of the cell around its longitudinal axis (Fig. 2.8). To better determine the cell apparent orientation, the horizontal

binarized cell image was rotated from -8.5° to 8.5° in 0.5° steps and the backbone determination and the sine fit were repeated after each rotation. The results of the sine fit (θ , ψ , L , A and λ) with the smallest χ^2 (the sum of the d^2 , where d is the vertical distances between the backbone points and the sine fit) value were saved. To speed up the image analysis process, this full procedure was only performed for the first 100 frames. In the rest of the frames, the values of A and λ were fixed to the average values \bar{A} and $\bar{\lambda}$ obtained from the first 100 fits, and only the parameters θ , ψ and L were determined.

When comparing the results of the measurement of the apparent orientation of the cells in the focal plane with either the sine fit or the elliptical fit for the same images, we found that there was on average a 3.2° difference in the value of θ . The error on θ (as estimated from the interpolated intercept of the OCF at $\tau = 0$ [41]) was smaller for the elliptical fit ($\epsilon = 0.96^\circ$ for the elliptical fit and $\epsilon = 1.45^\circ$ for the sine fit). The error on ψ , obtained with the sine fit was also estimated by the same method and found to be significantly larger, $\epsilon = 5.49^\circ$ on average.

The cell lengths obtained using both methods were strongly correlated, with the length measured using the elliptical fit (length of the major axis) on average 28% larger than that measured with the sine fit (end-to-end distance). We thus decided to use the median length obtained from the sine fits as the measurement of the cell length.

2.5 Orientation correlation functions

The orientation correlation function (OCF) corresponding to the apparent orientation of the cell in the focal plane is $C_\perp(\tau) = \langle \cos[\theta(t + \tau) - \theta(t)] \rangle$. $C_\perp(\tau)$

was calculated for each cell by averaging over all pairs of angles θ separated by a lag time τ . If the cell is confined to the focal plane and there is no magnetic field, $C_{\perp}(\tau)$ is expected to have an exponential form $C_{\perp}(\tau) = e^{-D_{r_{\perp}}\tau}$. This shows that at short times ($\tau \leq 1/D_{r_{\perp}}$), the cell keeps a memory of its orientation, but at longer times ($\tau \gg 1/D_{r_{\perp}}$), the orientation is completely randomized which leads to $C_{\perp}(\tau \gg 1/D_{r_{\perp}}) = 0$ [60]. $\tau_c = 1/D_{r_{\perp}}$ is the characteristic decay time inversely related to the transversal rotational diffusion coefficient $D_{r_{\perp}}$ [35]. Similarly, we defined the OCF relative to the orientation of the cell around its longitudinal axis as $C_{\parallel}(\tau) = \langle \cos[\psi(t + \tau) - \psi(t)] \rangle$, for which the form $C_{\parallel}(\tau) = e^{-D_{r_{\parallel}}\tau}$ is expected.

2.6 Limitations

When taking movies of the cell, we need to adjust the focus constantly to follow the cell, but sometimes we only caught part of the cell, which could cause errors in detected cell length and orientation. Before image analysis, we binarized and despeckled images from the movie, during this process, we could lose points on the periphery. In addition, different binary methods would give us different cell shape and orientation. The sine fit is noisy especially for short cells, and we only fitted the first 100 frames with varying A and λ , which could cause errors in the rotation around its long axis (ψ) measurement. Misalignment angle β is another factor could cause a error in ψ measurement as we can tell from the simulation, although we tried to correct this (Fig. 3.7d).

Chapter 3

Results and Discussion

We wanted to take advantage of both the typical helical geometry and the magnetic properties of *M. magneticum* cells to completely characterize their diffusion properties, and from them, infer the cells' drag coefficients in all four principal axes. In section 3.1, simulation results of measuring the rotational diffusion coefficients from angular trajectories are presented and discussed. In section 3.2 and 3.3, results of experimentally determined rotational and translational drag coefficients of *M. magneticum* cells are presented, respectively. In section 3.4, we present the finding of coupling between rotation and translation along the cell longitudinal axis. In section 3.5, the results of four principal drag coefficients are discussed.

3.1 Simulations results - measuring the rotational diffusion coefficients of cells from angular trajectories

Our first goal was to show the rotational diffusion coefficients could be determined from orientation correlation functions obtained in the presence of a magnetic field, and to determine the preferred experimental conditions to observe and characterize the rotational diffusion of *M. magneticum* cells. For this, we performed simulations of the rotational diffusion of a cell placed in an external magnetic field \vec{B} with varying intensity. In these simulations, the cell was represented by an elongated rigid particle (long axis \vec{L}) with a magnetic moment $\vec{\mu}$ (separated from \vec{L} by a fixed misalignment angle β). Details about the simulations can be found in section 2.1.

3.1.1 Orientation distributions

We first considered the case where $\vec{\mu}$ is exactly aligned with \vec{L} ($\beta = 0$). The apparent orientation of the particle in the focal plane, $\theta(t)$, was monitored throughout a simulation equivalent to a 2 s experiment. Examples of angular trajectories obtained for different magnetic field values are shown in Fig. 3.1a, where θ values are more restricted at higher fields. The orientation distributions for such a particle with rotations restricted to a plane is expected to follow a Boltzmann distribution with the form (Eq. 6 in Ref. [35]):

$$p(\theta) = e^{R \cos \theta} / [2\pi I_0(R)], \quad (3.1.1)$$

where I_n represents the modified Bessel function of the first kind of order n , and $R = \mu B/kT$ represents the balance between magnetic and thermal forces. By fitting the simulated orientation distributions with Eq. 3.1.1 (Fig. 3.1b), an estimate of R is obtained, and thus the value of μ is obtained if the value of B is known (Fig. 3.1c). Eq. 3.1.1 applies only to particles constrained to 2D rotations, thus the values of μ obtained from the fits of the θ distributions with this equation should become more accurate as B increases because the particles then pass from a free 3D rotation to a quasi-2D motion. Indeed, the simulations show that the measurement on μ becomes more precise as B increases (Fig. 3.1c). As the observed values of μ of *M. magneticum* AMB-1 cells fall in the range of $\mu \simeq 0.1 - 1.5 \times 10^{-15}$ A·m², a field $B > 0.1$ mT should sufficiently restrict cells in the focal plane such that Eq. 3.1.1 can be used to retrieve μ from the orientation distribution.

The orientation of the particle around its longitudinal axis, $\psi(t)$, was also monitored. The values of $\psi(t)$ are independent of the field B , as illustrated in Fig. 3.1d.

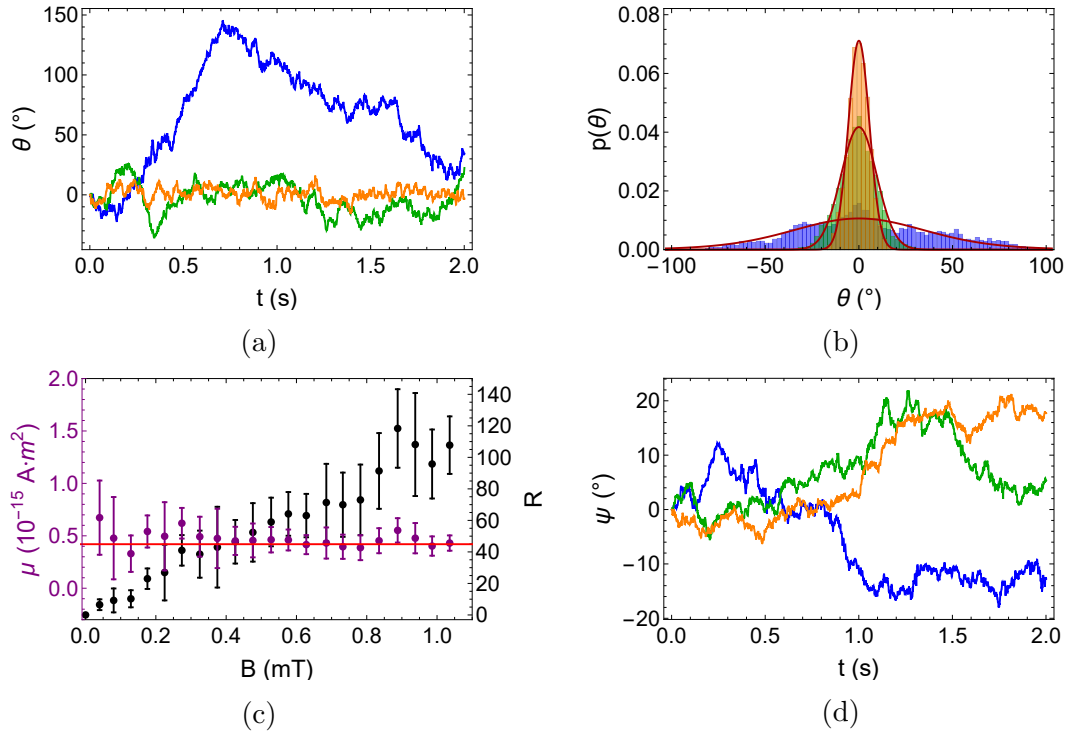


Figure 3.1: Orientation trajectories and distributions from simulations. (a) Examples of 2 s orientation trajectories $\theta(t)$ for simulated bacteria without external magnetic field (blue), for $B = 0.33$ mT (green) and for $B = 1$ mT (orange). (b) Orientation distributions for θ obtained as a result of 20 s simulations, with a fit to a simple Boltzmann distribution (Eq. 3.1.1). Same color scheme as in (a). (c) Values of μ (purple) and R (black) obtained from the fit of the θ distributions (the horizontal line represents the actual value of μ used in the simulation). (d) Examples of angular trajectories $\psi(t)$ for simulated bacteria. Same color scheme as in (a).

3.1.2 Orientation correlation functions


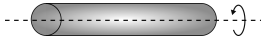
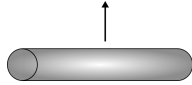
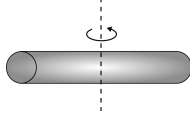
Parameter	Direction	Parameter	Direction
$D_{t_{\parallel}}$		$D_{r_{\parallel}}$	
$D_{t_{\perp}}$		$D_{r_{\perp}}$	

Table 3.1: The four principal diffusion coefficients of an elongated object.

One way to obtain the rotational diffusion coefficient $D_{r_{\perp}}$ (Table 3.1) of elongated particles such as bacteria is to calculate the orientation correlation function (OCF) $C_{\perp}(\tau)$ related to the particle's apparent orientation in the focal plane $\theta(t)$ [60]. When only thermal fluctuations influence the rotational diffusion and the diffusion is restricted in 2D, the OCF takes an exponential form. For the OCF, the characteristic decay time τ_c equals to the rotational diffusion persistence time $\tau_c = \tau_p = 1/D_{r_{\perp}} = f_{r_{\perp}}/kT$ (section 2.5, Eq. 1.2.19). In the presence of a magnetic field, however, the orientation of a MTB cell will become correlated at long time, and the characteristic persistence time τ'_c now depends also on the characteristic relaxation time ($\tau_r = f_{r_{\perp}}/\mu B$) and is expected to decrease [35]. An empirical expression for the OCF was proposed [35]:

$$C_{\perp}(\tau) = \left(1 - \frac{I_1(R)}{I_0(R)}\right)e^{-\tau/\tau'_c} + \frac{I_1(R)}{I_0(R)}. \quad (3.1.2)$$

At very short time ($\tau < \tau_r = f_{r_\perp}/\mu B$), the thermal motion is expected to dominate and the OCF should decay at the rate of $-D_{r_\perp}$ regardless of the R value. Thus, we should have $\tau'_c = (1 - \frac{I_1(R)}{I_0(R)})/D_{r_\perp}$. The simulated OCF has the expected form and can be fitted well with Eq. 3.1.2 (Fig. 3.2a). The fit returns both μ (from $R = \mu B/kT$) (Fig. 3.2c) and D_{r_\perp} (Fig. 3.2d). Similar to the case discussed in section 3.1.1, the values of μ and D_{r_\perp} obtained at very low field ($B < 0.1$ mT) are incorrect, because Eq. 3.1.2 was derived assuming a 2D trajectory. For $B > 0.2$ mT, a precise and accurate measurement of D_{r_\perp} is obtained (Fig. 3.2d, red symbols). The OCF might display correlated noise, thus, we also tried to only fit the OCF with a linear function for a short time range. This fitting method gives good result over a large range of B ($B = 0.1 - 0.5$ mT) when the fit is done over a small time range ($\tau = 0.001$ to 0.005 s) (Fig. 3.2d, black symbols).

The same analysis was done for the rotational diffusion of the cell around its longitudinal axis. As mentioned in section 3.1.1, this rotation is not affected by the field, thus, the OCF calculated from $\psi(t)$ is expected to decay exponentially to zero regardless of the field value (Fig. 3.3a). However, the OCF we calculate still has a strong dependence on the field. This is because the angle measured in the experiments and evaluated in the simulations (as the angle between the vector $\vec{\mu} - (\vec{\mu} \cdot \vec{L}/L^2)\vec{L}$ and a vertical plane $\vec{L} - z$ (section 2.1)), is not exactly $\psi(t)$, but rather an approximate value of ψ which is affected by any transversal rotation of the cell. This effect is stronger when \vec{L} is not aligned with the focal plane. Therefore, at low fields ($B < 0.5$ mT), the initial slope of the OCF is strongly affected, and its fitting with $C_{r_\parallel}(\tau) = e^{-D_{r_\parallel}\tau}$ returns the correct value for D_{r_\parallel} only when $B \geq 0.5$ mT by the fact that we are assimilating the estimated ψ to the actual ψ (Fig. 3.3c).

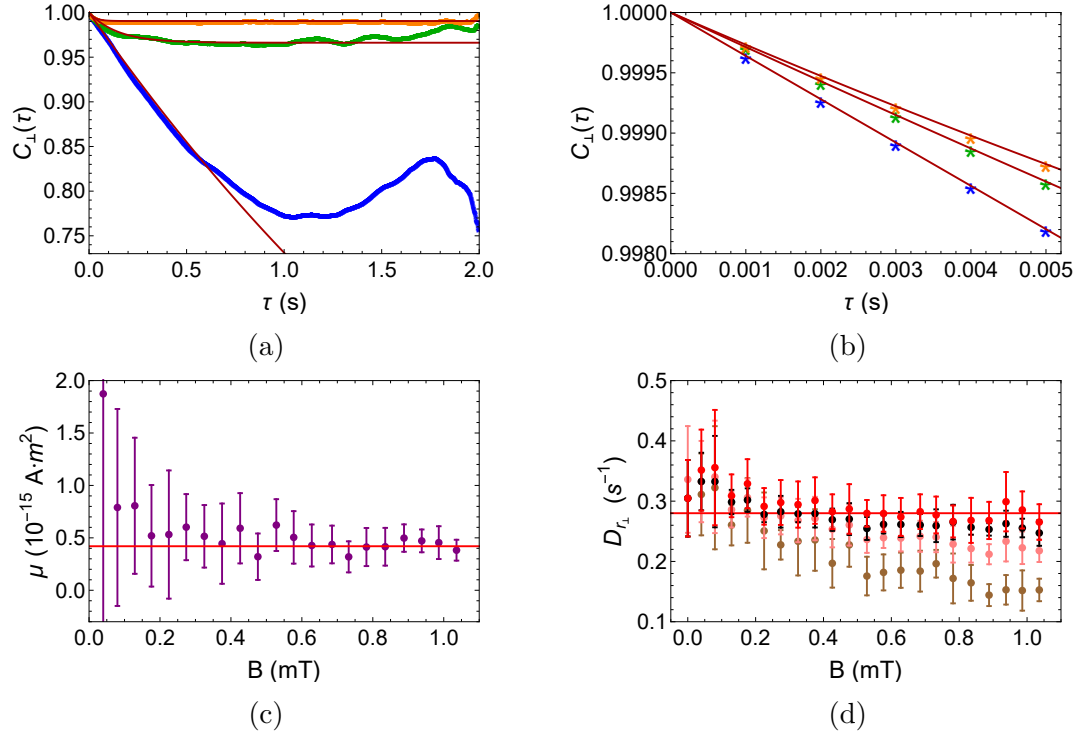


Figure 3.2: Results for rotation perpendicular to the cell longitudinal axis. (a) Orientation correlation functions for $\theta(t)$ at different fields, fit with Eq. 3.1.2 (exponential fit for no field situation). Blue symbols represent data simulated in the absence of an external magnetic field, green is for $B = 0.33$ mT and orange stands for $B = 1$ mT. (b) Close up of (a) on the short time range. (c) μ values obtained from fitting the OCF with Eq. 3.1.2 (the horizontal line represents the actual value of μ used in the simulation). (d) $D_{r_{\perp}}$ values obtained from fitting the OCF. Here, black, pink and brown symbols are for linear fits on the first 0.005 s, 0.015 s and 0.045 s of the OCF, respectively. The red symbols are the result of a fit on the first 0.045 s of the OCF with Eq. 3.1.2 (the horizontal line represents the actual value of $D_{r_{\perp}}$ used in the simulation).

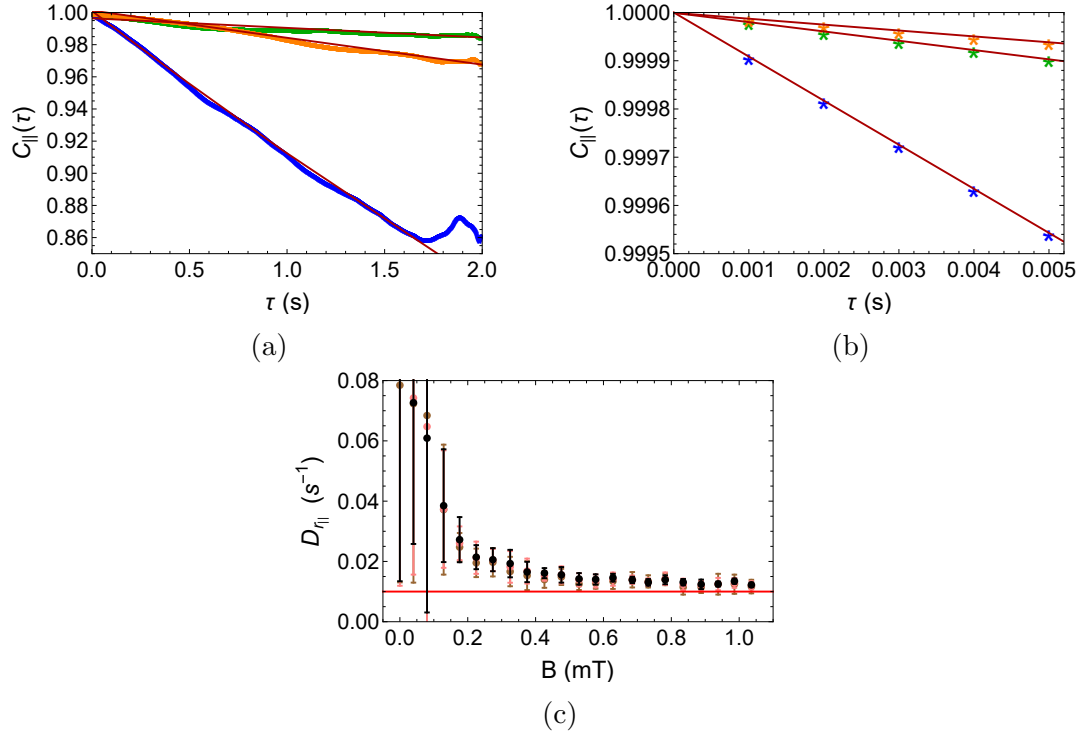


Figure 3.3: Results for rotation parallel to the cell longitudinal axis. (a) Orientation correlation functions for the estimated $\psi(t)$ at different fields with exponential fits. Blue symbols represent data simulated in the absence of an external magnetic field, green is for $B = 0.33$ mT and orange stands for $B = 1$ mT. (b) Close up of (a) on the short time range. (c) $D_{r_{\parallel}}$ values obtained from fitting the OCF. Here, black, pink and brown symbols are for exponential fits on the first 0.005 s, 0.015 s and 0.045 s of the OCF, respectively (the horizontal line represents the actual value of $D_{r_{\parallel}}$ used in the simulation).

3.1.3 Effect of measurement error

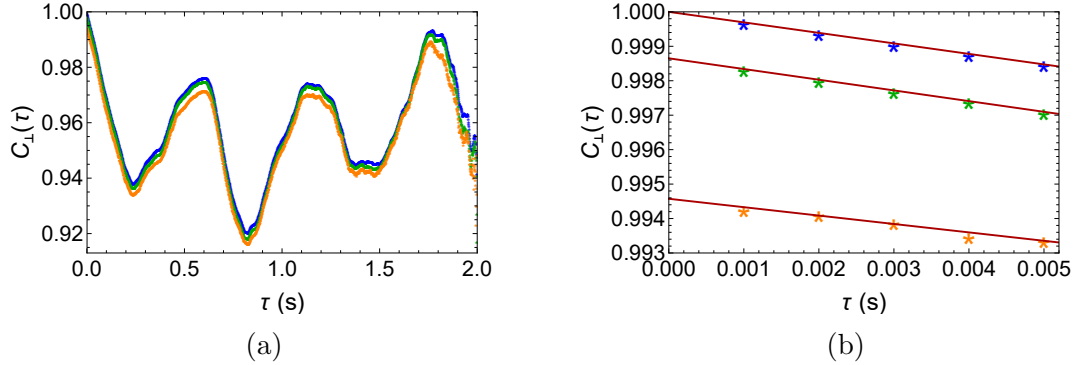


Figure 3.4: Influence of measurement noise on the OCF. (a) Three OCFs are shown, calculated from the same trajectory ($B = 0$), with either no noise added (blue curve), or noise added at each step on the measurement of the value of theta. The noise was drawn from a normal distribution with full width half maximum of 5° (corresponding to a variance $\sigma^2 = 0.00137 \text{ rad}^2$, green curve) or 10° (corresponding to a variance $\sigma^2 = 0.00549 \text{ rad}^2$, orange curve). (b) Close up of (a) on the short lag time range, brown lines are linear fit of the OCF.

The measurement error on the orientation of the bacteria is an important factor influencing the results of rotational diffusion experiments. If the measurement error, $\delta\theta$, has a Gaussian distribution with variance σ^2 , then the OCF becomes

$$C_{\perp}^N(\tau) = C_{\perp}(\tau) \times \langle \cos \delta\theta \rangle^2 \simeq C_{\perp}(\tau) \times (1 - \sigma^2). \quad (3.1.3)$$

This coincides with the OCF shifting downwards at the intercept of $\tau = 0$ by a value of σ^2 , and this is observed when noise is added in the simulations (Fig. 3.4).

3.1.4 Effect of a misalignment between cell axis and magnetic moment

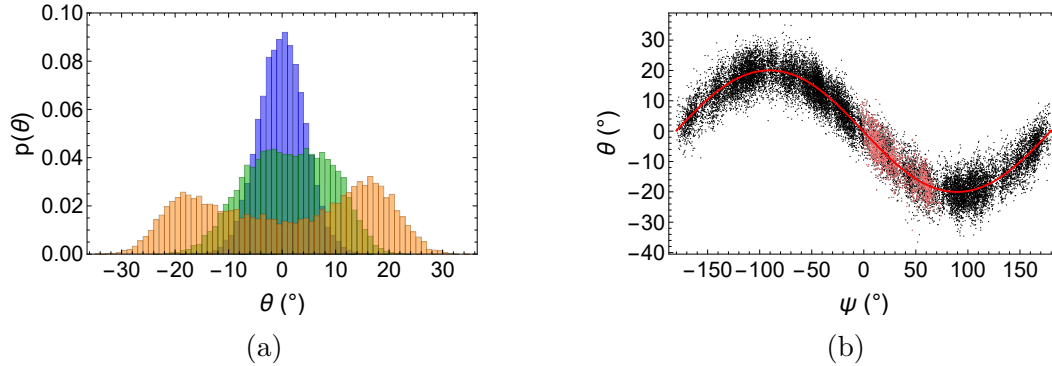


Figure 3.5: Influence of a misalignment between the cell longitudinal axis \vec{L} and its magnetic moment $\vec{\mu}$. (a) Influence of misalignment on simulated orientation distributions in a magnetic field $B = 1$ mT. Here, the misalignment angles for blue, green and orange distributions are $\beta = 0^\circ$, $\beta = 10^\circ$ and $\beta = 20^\circ$, respectively. (b) Coupling between the apparent orientation in focal plane, θ , and the apparent orientation around the cell longitudinal axis, ψ , for a misalignment angle $\beta = 20^\circ$. The pink points show the result from the first 2 s of the simulation. The red curve is the fit to the black points in the form of Eq. 3.1.4.

When cells are placed in a magnetic field, another factor likely of affecting the angular traces and OCF is the misalignment (β) between the cell longitudinal axis (\vec{L}) and its magnetic moment ($\vec{\mu}$). As mentioned in section 1.1.5, it has been found that the angle between these two vectors was on average $\beta = 6^\circ$ and up to 20° for individual *M. magneticum* cells [41]. Simulated cells with misalignment behave just like cells observed in experiments with a magnetic field. Cells with a small misalignment have single-peak distributions centered around $\theta = 0$ (as already seen in Fig. 3.1b), however, as β becomes larger, the distributions split into two symmetric peaks distributions (Fig. 3.5a).

For a non-zero β and in the presence of a strong magnetic field, the rotation of the

cell around its longitudinal axis (ψ) is coupled with a rotation due to the magnetic torque ($\vec{\mu}$ to be aligned with \vec{B}), resulting in θ and ψ being coupled in a specific way:

$$\theta(\psi) = \tan^{-1}(\tan \beta \cdot \cos(\psi + \delta)), \quad (3.1.4)$$

where δ is a geometrical phase shift (Fig. 3.5b) [41]. The coupling between θ and ψ has an interesting consequence for the OCF, as there are now two characteristic relaxation times associated with changes in the orientation, the rotational diffusion relaxation time $\tau_c = 1/D_{r_\perp}$ and the relaxation time associated with rotation around the cone ($\vec{L} - \vec{\mu}$ cone), $\tau_r = f_{r_\perp}/\mu B$. As shown in Fig. 3.5b, rotational diffusion relaxation is achieved in less than 2 s (the usual length of a simulation), whereas capturing the relaxation around the cone (which involves both a rotation perpendicular and a rotation parallel to the cell longitudinal axis) takes longer, and requires running a longer simulation (thus $\tau_r > \tau_c$). Therefore, the OCF of cells with a strong misalignment and placed in a magnetic field displays two characteristic decay times (Fig. 3.6a). Fitting this kind of OCF up to a longer times, although possible and interesting since it would yield the value of μ (Fig. 3.6c), would require us to perform longer experiments. Fortunately, it is always possible to fit such OCF only at a very short time ($\tau \leq 5$ ms), in a region where the decay is linear and equal to $-D_{r_\perp}$ (Fig. 3.6d).

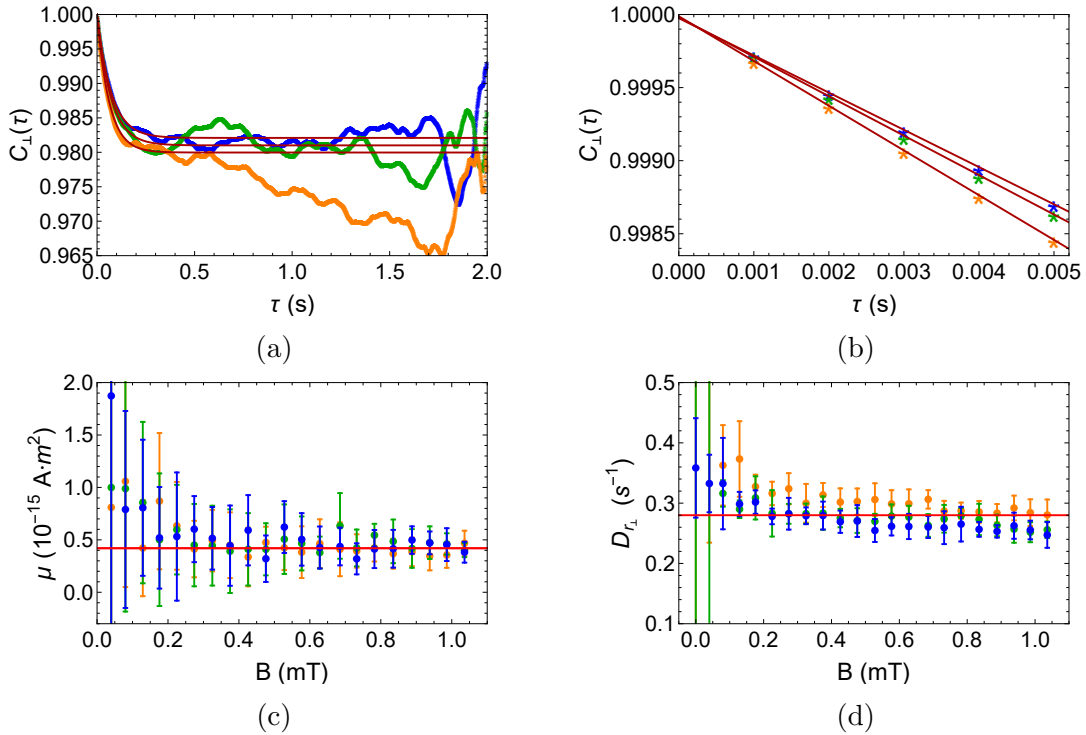


Figure 3.6: Results of simulations done for cells with different misalignment angles for the rotation perpendicular to the cell longitudinal axis. (a) Influence of misalignment on OCF for rotation perpendicular to the cell longitudinal axis: Example of OCF for the misalignment angles $\beta = 0^\circ$ (blue), $\beta = 10^\circ$ (green) and $\beta = 20^\circ$ (orange) with external magnetic field $B = 0.53$ mT. (b) Close up of (a) on the short time range. (c) μ values obtained from fitting the OCF with Eq. 3.1.2 for 0.045 s for different misalignment angles. Same color scheme as in (a) (the horizontal line represents the actual value of μ used in the simulation). (d) $D_{r_{\perp}}$ values obtained from fitting the OCF with a line for 0.005 s for different misalignment angles. Same color scheme as in (a) (the horizontal line represents the actual value of $D_{r_{\perp}}$ used in the simulation).

The consequences of a misalignment are even more drastic for the OCF associated with $\psi(t)$, since at high magnetic fields, the axis of the cell can still be far from the focal plane. In addition, the coupling between rotation of the cell perpendicular to its longitudinal axis and the measured value of ψ always exists, leading to a quicker decay of the OCF (Fig. 3.7a,b), and an overestimated value of $D_{r_{\parallel}}$, even with high magnetic fields (Fig. 3.7c). Thus, we examined the relation between $D_{r_{\parallel}}$ (obtained

by fitting an exponential function for 0.045 s) and the misalignment angle β , and we found a quadratic relation (Fig. 3.7d). The fit

$$D_{r_{\parallel}} = 0.01 + 0.0002\beta + 0.00007\beta^2 \quad (3.1.5)$$

was then used to correct our experimental data, and this correction was later refereed as the misalignment factor.

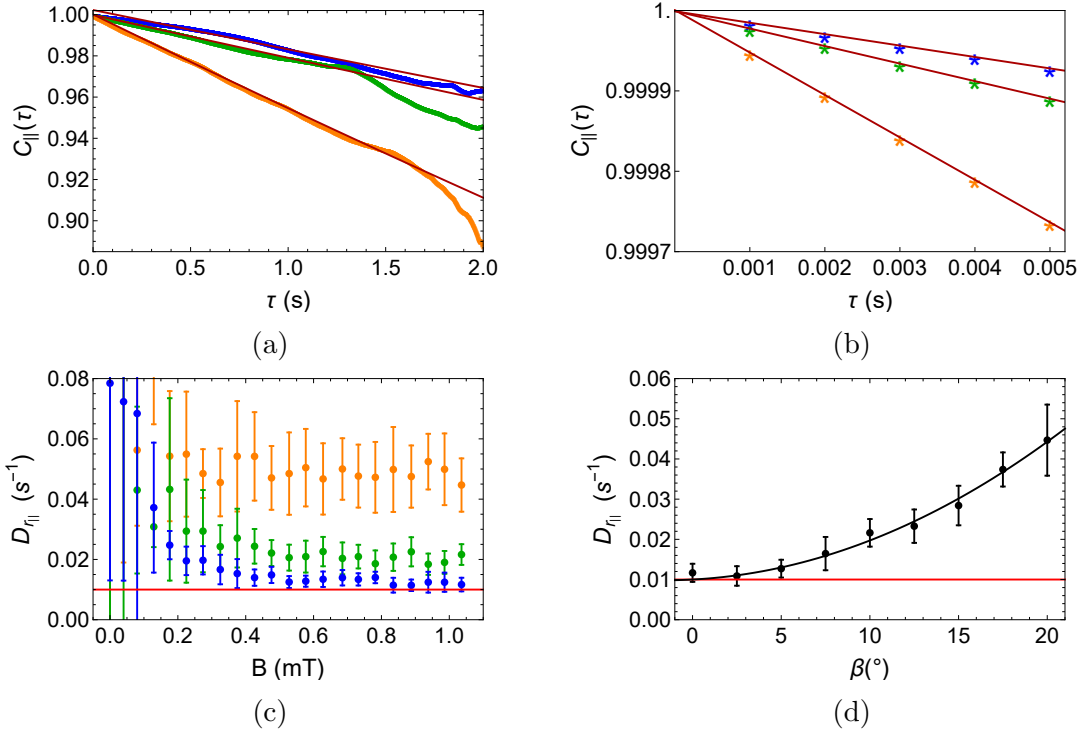


Figure 3.7: Results of simulations with different misalignment angles for rotation parallel to the cell longitudinal axis. (a) Influence of misalignment on OCF for rotation parallel to the cell longitudinal axis: Example of OCF for the misalignment angles $\beta = 0^\circ$ (blue), $\beta = 10^\circ$ (green) and $\beta = 20^\circ$ (orange) with external magnetic field $B = 0.53$ mT. (b) Close up of (a) on the short time range. (c) $D_{r_{\parallel}}$ values obtained from fitting the OCF with an exponential function for 0.045 s for different misalignment angles. Same color scheme as in (a) (the horizontal line represents the actual value of $D_{r_{\parallel}}$ used in the simulation). (d) Relation between the apparent measured $D_{r_{\parallel}}$ for external magnetic field $B = 1$ mT and the misalignment angle β . Red curve is a quadratic fit to the data points (Eq. 3.1.5).

3.2 Experimental determination of *M. magneticum* rotational drag coefficients

3.2.1 Rotation perpendicular to the cell longitudinal axis

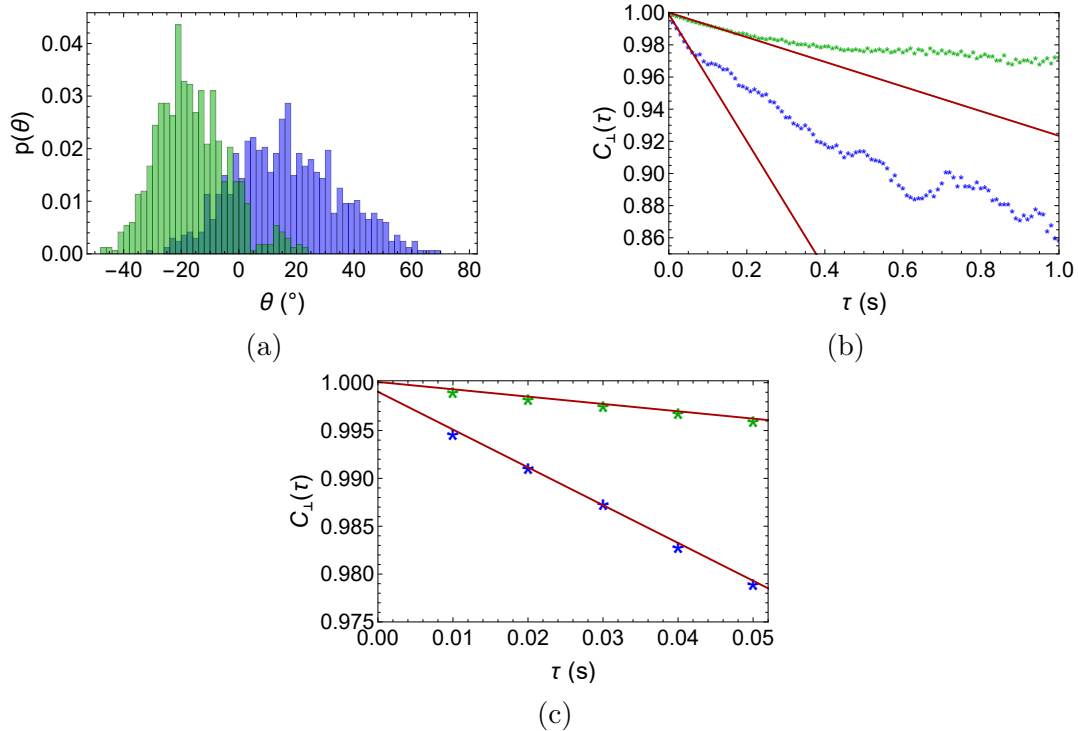


Figure 3.8: Examples of orientation distribution and OCF for rotation perpendicular to the cell longitudinal axis for two cells of different lengths. (a) Examples of orientation distributions (angle θ) obtained for a short $1.6 \mu\text{m}$ -long cell (blue bars) and a long $3.8 \mu\text{m}$ -long cell (green bars) for 8.38 s placed in an external field $B = 0.1 \text{ mT}$. (b) Corresponding OCF and linear fits based on the first 0.05 s of the OCF. Same color scheme as in (a). (c) Close up of (b) on the short time range.

In order to obtain the drag coefficient corresponding to the cell rotation perpendicular to its longitudinal axis, $f_{r_{\perp}}$, the motion of $n = 35$ and $n = 31$ different *M. magneticum* AMB-1 cells at low magnetic fields ($B = 0.1 \text{ mT}$ and $B = 0.23 \text{ mT}$) were

recorded. These were chosen as our simulations suggested that $B = 0.1 - 0.5$ mT was an optimal trade-off between ensuring that the motion of the bacteria was more or less constrained to the focal plane and ensuring that $\vec{\mu}$ was still able to fluctuate around \vec{B} . Since the effective viscosity, η , is larger when the bacteria are close to the glass than in the bulk, we only imaged cells more than $20 \mu\text{m}$ away from the coverslip or glass slide, which should be enough for them to have no interaction with the glass [61]. The orientation of the cells in the focal plane, θ , was obtained from an elliptical fit of the cell in each available movie frame. The traces, orientation distribution and OCF were generated for each cell (examples of which are shown in Fig. 3.8 for cells of different lengths). Because the misalignment between \vec{L} and $\vec{\mu}$ was observed for most cells (see the example orientation distributions in Fig. 3.8a, which are not centered around $\theta = 0$ because of a misalignment combined with a measurement of a short duration), only the first 0.05 s of the OCF were analyzed using a linear fit (Fig. 3.8b,c).

For each cell, an average length L was calculated, as the median value of all the different end-to-end lengths measured in each frame (section 2.4). We found that most cells have a length between $L = 2$ and $4 \mu\text{m}$, as shown in previous studies [35, 41]. After the addition of $10 \mu\text{g/mL}$ cephalixin, the average cell length increased as expected, and fell in the range of $L = 3.5 - 6 \mu\text{m}$. The value of $f_{r_{\perp}}$ (the rotational drag coefficient perpendicular to the cell longitudinal axis), as well as σ (the standard deviation of the error made on the angle θ), were obtained from the linear fit of the first 0.05 s of the OCF. $f_{r_{\perp}}$ is well described by a power law, $f_{r_{\perp}} = 3.95 L^{2.15}$, with $f_{r_{\perp}}$ in the unit of $\text{fN}\cdot\mu\text{m}\cdot\text{s}$ and L in μm (Fig. 3.9a). The measured values of $f_{r_{\perp}}$ for *M. magnetospirillum* cells are very close to that expected for a cylinder of fixed $0.65 \mu\text{m}$

radius (average semi-minor axis length from elliptical fits of the cells), and most experimental points fall within the predictions for cylinders with radii 20% smaller or larger. The values predicted for an ellipsoid with the same $0.65 \mu\text{m}$ radius coincide with the lower bound of the experimental data points. The error on the measurement of the cell orientation, σ , decreases as cell length L increases (Fig. 3.9b), which implies a more accurate determination of the cell orientation with the elliptical fits for longer cells.

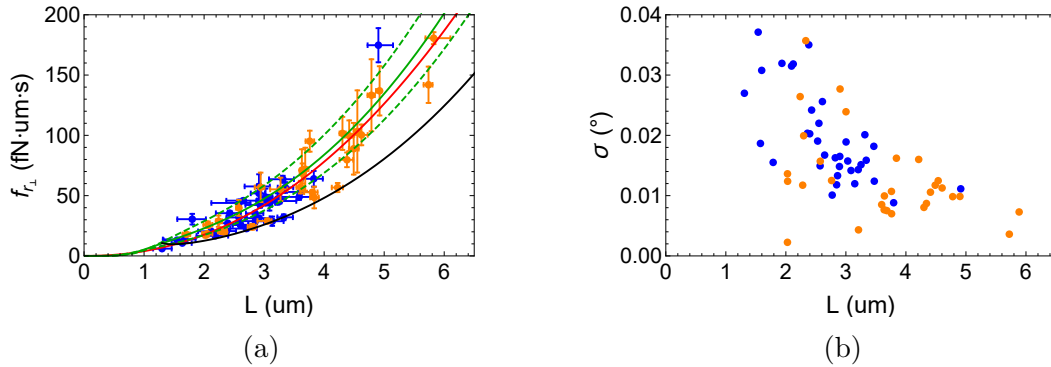


Figure 3.9: Experimentally determined values of the rotational drag coefficient perpendicular to the longitudinal axis of *M. magneticum* cells. (a) Measured $f_{r_{\perp}}$ as a function of cell length. Blue data was obtained at 40 \times magnification with $B = 0.1$ mT and orange data at 100 \times magnification with $B = 0.23$ mT. The error bars for L come from the first quartile and the third quartile of the length over the entire movie, and the error bars on $f_{r_{\perp}}$ come from the standard deviation of $f_{r_{\perp}}$ obtained from different fitting times of the OCF. The red curve is a power law fit of the data, green curves represent theoretical predictions for cylinders of radius $0.8r$ (lower dashed), r (solid) or $1.2r$ (upper dashed) ($r = 0.65 \mu\text{m}$). The black curve represents the theoretical prediction for an ellipsoid of radius r . (b) Standard deviation of the error on θ (denoted σ and obtained from the intercept of the OCF), as a function of cell length. Same color scheme as in (a).

3.2.2 Rotation around the cell longitudinal axis

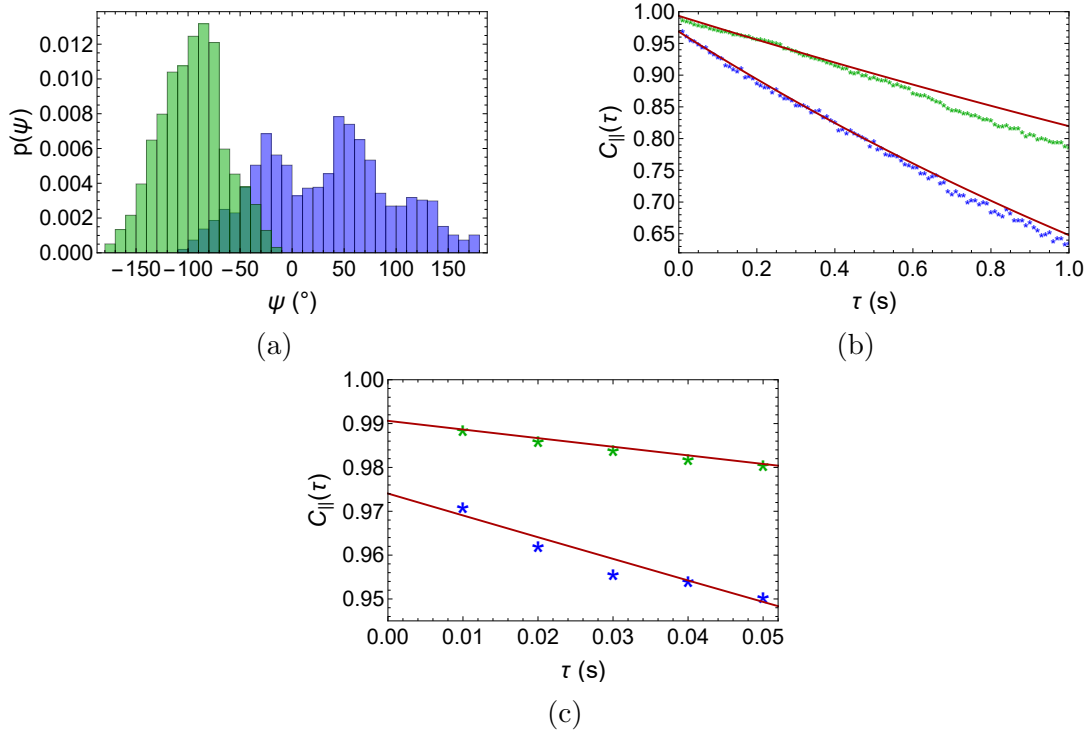


Figure 3.10: Examples of orientation distribution and OCF for rotation around the cell longitudinal axis for two cells of different lengths. (a) Examples of angular distributions obtained for a short (blue) ($2.37 \mu\text{m}$ long) and a long bacteria (green) ($5.47 \mu\text{m}$ long) for 21 s at $B = 1 \text{ mT}$. (b) Corresponding OCF and exponential fits for the first 0.45 s of the OCF. Same color scheme as in (a). (c) Close up of (b) on the short time range with exponential fits for the first 0.05 s of the OCF.

In order to study the rotation of the cell around its longitudinal axis, the experiment protocol was modified in two ways. First, we used higher magnetic field ($B = 1 \text{ mT}$, $n = 44$ obtained at $40\times$ magnification and $n = 31$ obtained at $100\times$ magnification), since the simulations suggested that only for $B > 0.5 \text{ mT}$ could the real value of the rotational diffusion coefficient around the longitudinal axis, $D_{r_{||}}$, be correctly estimated from the fit of the OCF. Second, a more complex fitting procedure was applied to the images, which involved determining the position of the projection of

the cell backbone in the focal plane and fitting it to a sine function. This allowed the estimation of the orientation of the cell around its longitudinal axis, ψ (see section 2.4 for details). Examples of orientation distributions and OCF associated with ψ are shown in Fig. 3.10. From the intercept of the OCF at $\tau = 0$, it is clear that the error made on ψ is much larger than the one made on θ , and also that this error increases as L decreases (Fig. 3.11b). Fitting the OCF with an exponential function, and then taking into account the misalignment factor returns an estimate for $f_{r_{\parallel}}$ (Fig. 3.11a). Cells with misalignment angle $\beta \geq 9.5^\circ$ were omitted from the results since inaccurate estimates were returned for cells with large misalignment angles, as shown in simulations (section 3.10). The rotational drag coefficient parallel to the cell longitudinal axis as a function of cell length was fitted with a line, $f_{r_{\parallel}} = 2.77 + 3.67L$. Since the error on ψ is larger, the result for $f_{r_{\parallel}}$ are noisier than for $f_{r_{\perp}}$. The cylinder and ellipsoid predictions have similar trends as the data points.

Along with the cell length, the sine fit method returned additional structural parameters, the wavelength (λ) and amplitude (A) of the cell backbone (Fig. 2.8), which were found to vary very little across the population. With the $40\times$ objective, we measured $\lambda = 2.55 \pm 0.25 \mu\text{m}$ and $A = 0.20 \pm 0.04 \mu\text{m}$ (mean \pm stdv, $n = 44$), and with the $100\times$ objective, we obtained $\lambda = 2.23 \pm 0.30 \mu\text{m}$ and $A = 0.21 \pm 0.04 \mu\text{m}$ (mean \pm stdv, $n = 31$). Hylemon et al. studied the morphology of the genus *Spirillum*, and the range of cell wavelength they found was $\lambda = 1.8 - 20 \mu\text{m}$ [62]. The wavelength of our AMB-1 cells is in the range and close to the lower bound.

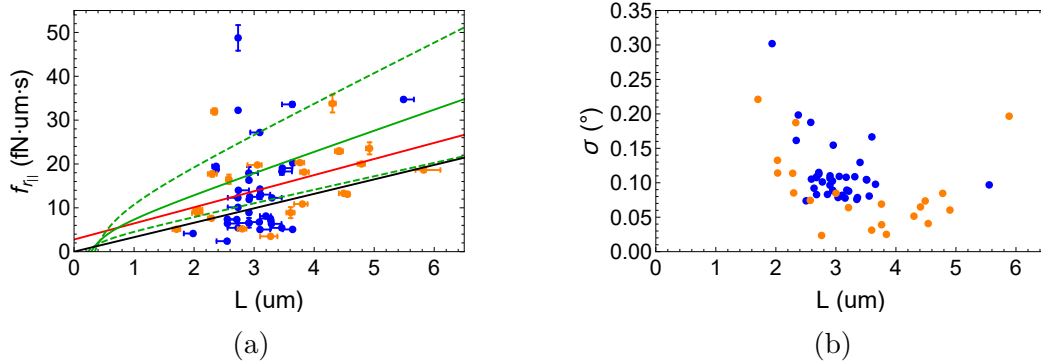


Figure 3.11: Experimentally determined values of the rotational drag coefficient around the longitudinal axis of *M. magneticum* cells. (a) Measured $f_{r||}$ as a function of cell length for $B = 1$ mT. Blue data was obtained at 40 \times magnification and orange data at 100 \times magnification. The red curve is a linear fit, green curves represent theoretical predictions for cylinders of radius $0.8r$ (lower dashed), r (solid) or $1.2r$ (upper dashed) ($r = 0.65 \mu\text{m}$) and the black curve represents the theoretical prediction for an ellipsoid of radius r . (b) Standard deviation of the error on ψ (denoted σ and obtained from the intercept of the OCF), as a function of cell length. Same color scheme as in (a).

3.3 Experimental determination of *M. magneticum* translational drag coefficients

The data obtained at high field also gives the opportunity to estimate the two principal translational drag coefficients of the cells, since constraining the direction of the cell longitudinal axis to be along the direction of the external magnetic field separates diffusion along and perpendicular to the cell longitudinal axis. Typical traces and distributions of displacements both along (x - direction) and perpendicular (y - direction) to the cell longitudinal are shown in Fig. 3.12a-f for two cells with different lengths. As expected, there is no correlation observed between the displacements along these two directions. The distributions of displacements are Gaussian, pointing

(as expected) to a simple diffusion process. The mean-squared-displacement (MSD) as a function of lag time was calculated for each cell in both directions (examples are shown in Fig. 3.12g), and the slope of these MSD at short time returned the corresponding translational diffusion coefficients, from which translational drag coefficients along and perpendicular to the cell longitudinal axis were calculated. The results are shown in Fig. 3.13.

The translational drag coefficient perpendicular to the cell longitudinal axis as a function of cell length was fitted with a line, $f_{t\perp} = 6.21 + 3.12L$. Comparing this with the values predicted for either a cylinder or an ellipsoid of radius either $0.65 \mu\text{m}$ (measured average semi-minor axis length from elliptical fits of the cells, “ R ” in Fig. 2.7) or $0.27 \mu\text{m}$ (measured average radius of helical cells’ images, “ r ” in Fig. 2.8), all curves have a similar trend, most of the experimental points lay between the values predicted for those two radii. The cylinder prediction with $r = 0.27 \mu\text{m}$ is the curve closest to the linear fit of the data. For the translational drag coefficient parallel to cell longitudinal axis, we obtained a linear fit, $f_{t\parallel} = 7.37 + 1.81L$. Similar to $f_{t\perp}$, we compared this to predictions for a cylinder and an ellipsoid, and that for a cylinder with $0.27 \mu\text{m}$ radius still gives us the closest result to the linear fit of the data. Most data points lay between two ellipsoid predictions, but the cylinder prediction with radius of $0.65 \mu\text{m}$ overestimated $f_{t\parallel}$ value. There is a correlation between $f_{t\perp}$ and $f_{t\parallel}$, as $f_{t\parallel}$ increases as $f_{t\perp}$ increases, as predicted by all the models considered (Fig. 3.13c). From the point of view of its translational drag coefficients, *M. magneticum* cells behave mostly like an ellipsoid with the same length as the cell and a radius in between the radius of the cell body ($\approx 0.27 \mu\text{m}$) and the external radius of the helix described by this body ($\approx 0.65 \mu\text{m}$).

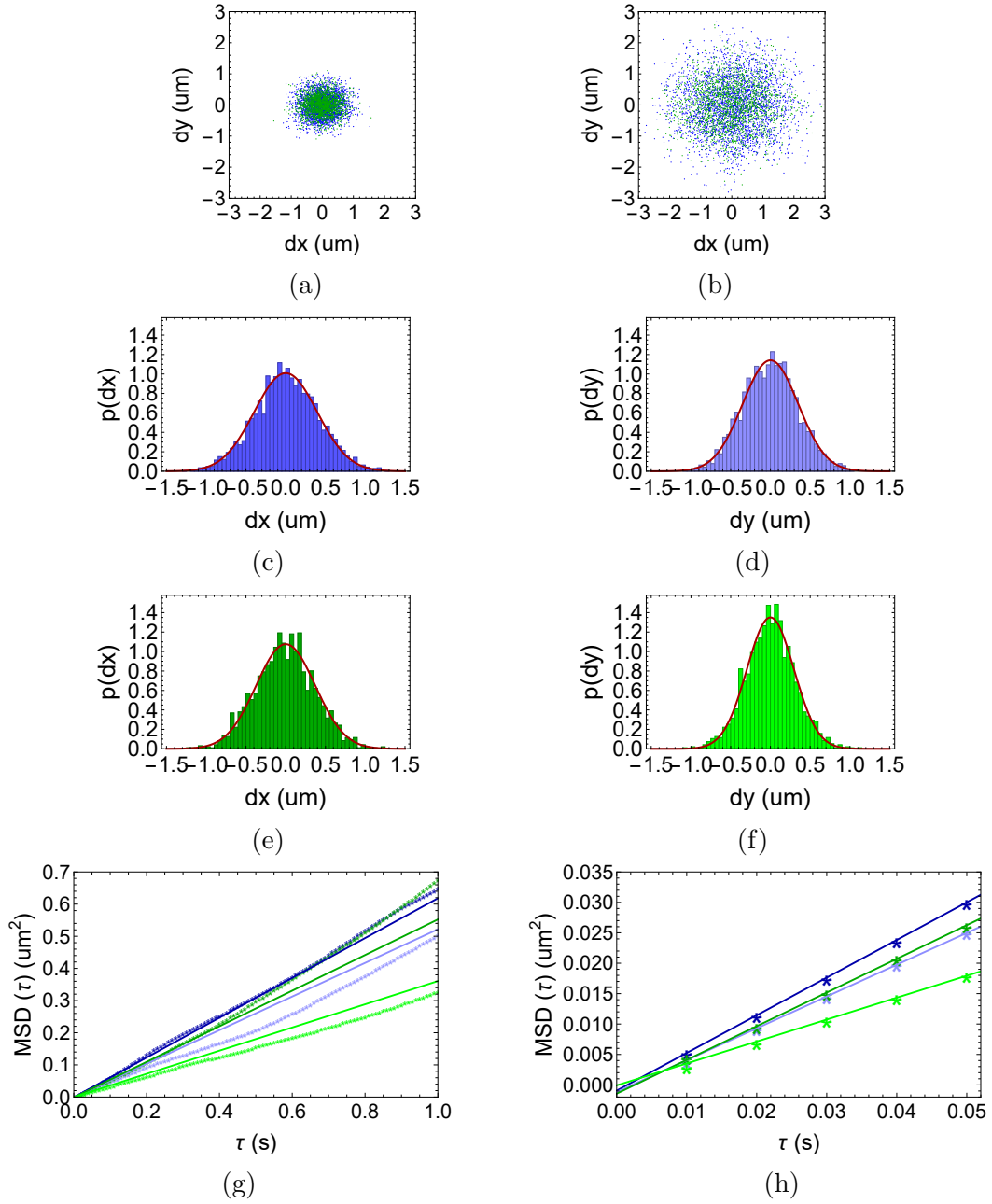


Figure 3.12: Translational diffusion. (a) Displacements observed for a short (blue) ($L = 2.37 \mu\text{m}$) and a long (green) ($L = 4.37 \mu\text{m}$) bacteria at $B = 1 \text{ mT}$ after $\tau = 0.01 \text{ s}$. (b) Displacements for the same bacteria at $B = 1 \text{ mT}$ after $\tau = 0.05 \text{ s}$. (c-f) Distribution of displacements in x - (darker color) and y - (lighter color) directions for the short (blue) and long (green) cell after $\tau = 0.01 \text{ s}$. (g) Corresponding MSD and linear fit for 0.05 s . Same color scheme as in (c-f). (e) Close up of (g) on the short time range.

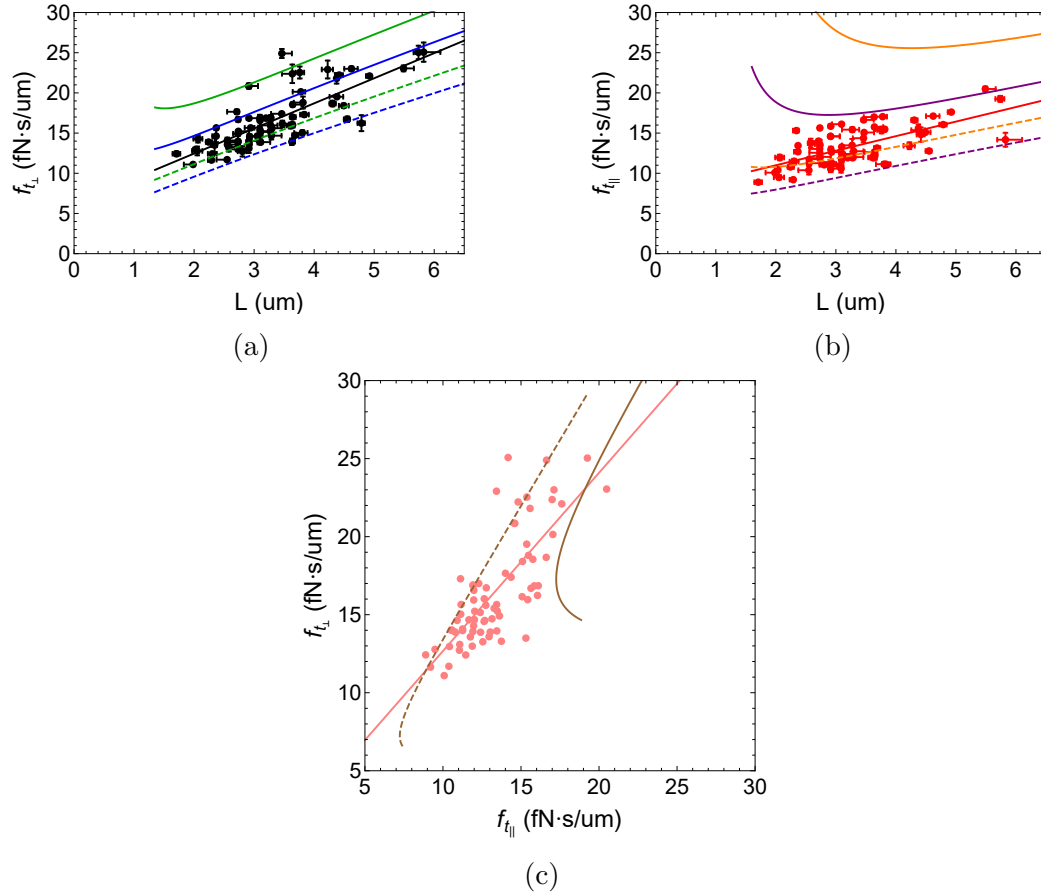


Figure 3.13: Experimentally determined translational drag coefficients of *M. magneticum* cells. (a) Translational drag coefficient perpendicular to the cell long axis, $f_{t\perp}$, as a function of cell length. The error bars on the length come from the first quartile and the third quartile of the length over entire movie, and the error bars on f_t are the standard deviation of values obtained from the fit of the mean-squared-displacement over different time ranges. The solid black line is a linear fit of the data. The green curves represent theoretical predictions for cylinders of radius 0.65 μm (solid) or 0.27 μm (dashed) and the blue curves represent theoretical predictions for ellipsoids of radius 0.65 μm (solid) or 0.27 μm (dashed). (b) Translational drag coefficient parallel to the cell long axis, $f_{t\parallel}$, as a function of cell length. The solid red line is a linear fit of the data. The orange curves represent theoretical predictions for cylinders of radius 0.65 μm (solid) or 0.27 μm (dashed) and the purple curves represent theoretical predictions for ellipsoids of radius 0.65 μm (solid) or 0.27 μm (dashed). (c) $f_{t\parallel}$ vs. $f_{t\perp}$ with a linear fit (pink line). The brown curves represent theoretical predictions for ellipsoids of radius 0.65 μm (solid) or 0.27 μm (dashed).

3.4 Coupling between rotation and translation along the cell longitudinal axis

The fluctuation in the orientation of cylinders are decoupled from their translational motions [63, 64], so rotations and translations can be treated separately. However, this is not the case for chiral objects, such as the helical *M. magneticum* AMB-1 cells. For a helical object, we expect a coupling between the rotation around and translation along the helical axis. A coupling drag coefficient, f_c , quantifies this coupling behavior.

3.4.1 Handedness of *M. magneticum* cells

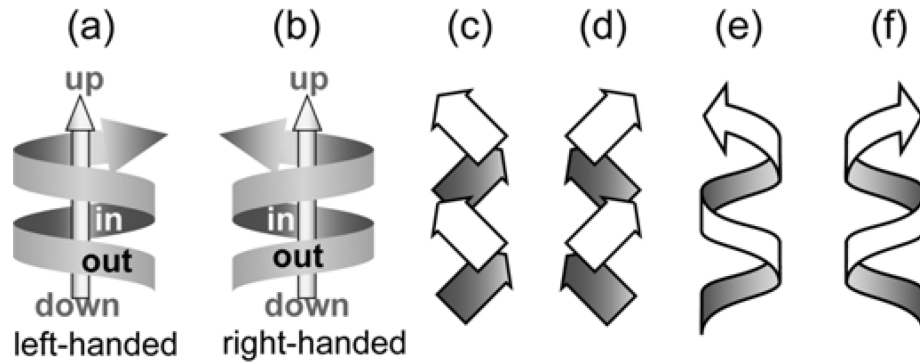


Figure 3.14: Right- and left-handed helices. (a), (c) and (e) represent left-handed helices. (b), (d) and (f) represent right-handed helices. Reproduced from [65].

f_c depends on the shape and size of the object and the viscosity of the surrounding fluid as other drag coefficients, but it also depends on the handedness of the object (Fig. 3.14). We therefore wanted to find out whether AMB-1 cells were left- or right-handed. By fluorescently labeling a fixed protein on an AMB-1 cell, and following the rotation of the label, Murat et al. obtained a trajectory of the cell body by tracking

that [50]. They concluded that the cells were right-handed since they observed that the cell moved away from the observer rotating clockwise. However, Schmitzer et al. used optical traps to capture *M. magneticum* cells vertically in focus and observed them rotating clockwise in the optical traps, and they concluded that AMB-1 cells were left-handed [66]. In addition, Konishi and Yoshii studied several *Aquaspirillum* by scanning electron microscopy and showed that some species were right-handed and some were left-handed [67].

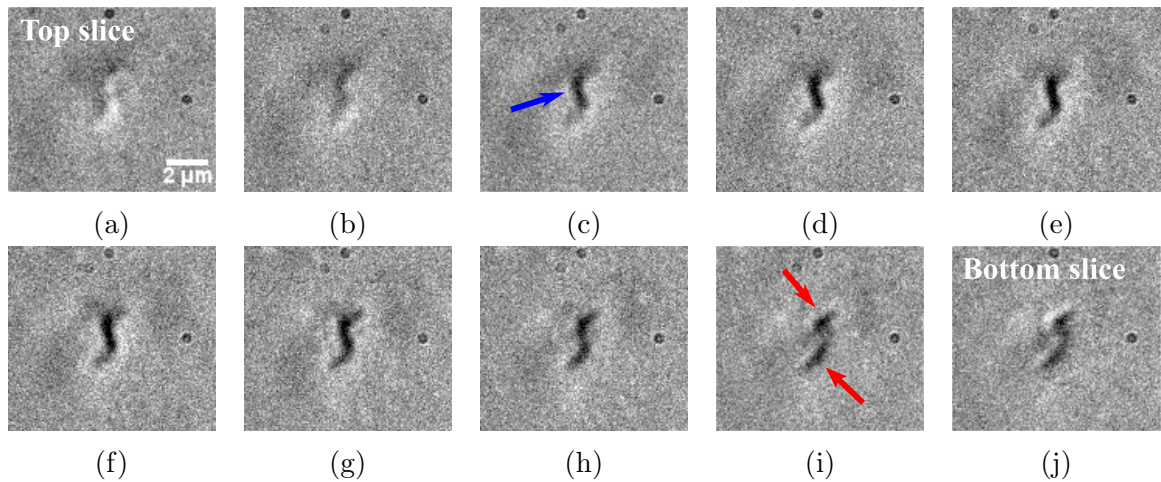


Figure 3.15: z - stack images of a cell stuck on glassslide. (a) - (j): Images from the top slice of the cell to the bottom slice of the cell (vertical steps: $0.5 \mu\text{m}$). The blue arrow in (c) indicates the middle part of the cell. The red arrows in (i) indicate the edge parts of the cell.

We studied the handedness of the cells in our culture by taking z - stack images of cells stuck on the glass slide. As shown in Fig. 3.15, from the top to the bottom, we saw that the middle part of the cell first and then two edge parts, and it was orientated from the right to the left as we went along the cell axis, thus, we concluded this cell was left-handed. All the cells we observed were left-handed, contradicting the result of Murat et al., but agreeing to the result of Schmitzer et al.. To confirm our results,

and as an improvement of this experiment, we could apply a vertical magnetic field and fix the cells vertically in a gel, then image them again in the z - direction to directly observe the helix rotation. In addition, we could obtain information about the cells' handedness by imaging live cells close to the glass slide because when cells are swimming close to an interface, they will go in circles (a hydrodynamic effect) and the direction of their circular trajectory is related to the cell's handedness [44, 61].

3.4.2 Experimental detection of coupling between the rotation around and translation along the cell longitudinal axis

We indeed detected such a coupling for individual *M. magneticum* cells, as evidenced by a correlation between displacement along the cell longitudinal axis and rotation along that axis, as shown in Fig. 3.16a. The coupling exists across the cell population, and the slope of $dx/d\psi$ increases linearly as normalized cell length (L/λ) increases (Fig. 3.16b).

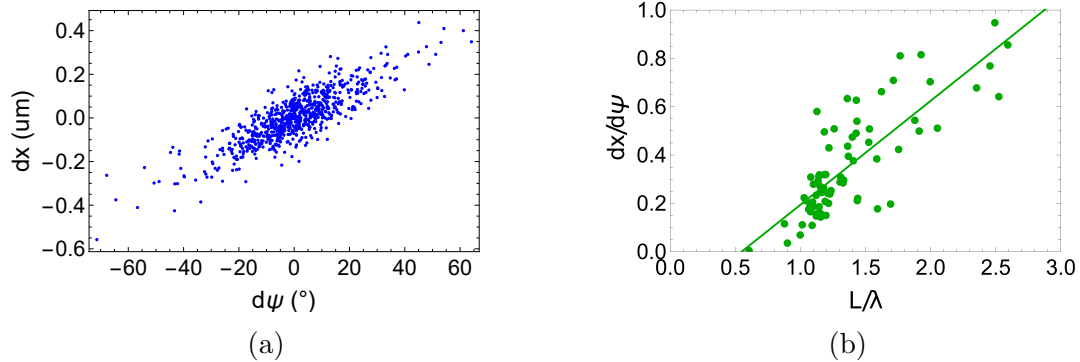


Figure 3.16: Results of coupling between rotation around (ψ) and translation along (x) the cell longitudinal axis. (a) An example of strong coupling between dx and $d\psi$ for a single cell (each point represents a single step in the cell trajectory). (b) $dx/d\psi$ (the slope of the linear fit of dx vs. $d\psi$ data, for example, (a)) as a function of normalized cell length with a linear fit.

3.5 Comparison of different drag coefficients

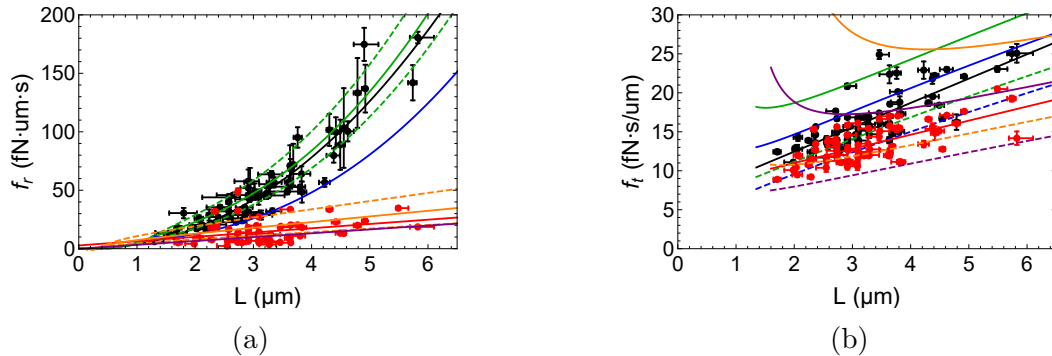


Figure 3.17: Dependence of drag coefficients on cell length. (a) Dependence of rotational drag coefficient on cell length. Black points represents $f_{r\perp}$ data (Fig. 3.9a) and red points represents $f_{r\parallel}$ data (Fig. 3.11a). Black curve is the power law fit in Fig. 3.9a, green curves are the same cylinder predictions as in Fig. 3.9a and blue curve is ellipsoid prediction in Fig. 3.9a. Similarly, red line is the same linear fit as in Fig. 3.11a, orange curves are the cylinder predications and purple curve is the ellipsoid prediction in Fig. 3.11a. (b) Dependence of translational drag coefficient on cell length. Same plot scheme as in Fig. 3.13a,b.

Comparing $f_{r\perp}$ and $f_{r\parallel}$ in Fig. 3.17a, generally, $f_{r\perp}$ is higher than $f_{r\parallel}$ for a certain cell. This result indicates that the cell is easier to rotate around itself than moving perpendicular to its longitudinal axis, which is expected for a small elongated particle. In addition, $f_{r\perp}$ is increasing faster than $f_{r\parallel}$ as cell length increases, which means cell length has a more significant effect on $f_{r\perp}$. Similar to f_r , comparing $f_{t\perp}$ and $f_{t\parallel}$ in Fig. 3.17b, generally, $f_{t\perp}$ is higher than $f_{t\parallel}$ for a certain cell, which is also expected for a small elongated particle. Comparing f_r and f_t , different cell shape parameters matter more; for f_r , the overall shape of the cell is more important, but the exact shape of cell matters more for f_t .

In 2017, Zahn et al. applied Stokesian dynamics and Boundary Integral Method to calculate the translational and rotational viscous drag coefficients using individual *Magnetospirillum gryphiswaldense* (MSR-1) bacterium's end-to-end-length, arc length, amplitude and diameter [68]. AMB-1 and MSR-1 belong to the same genus *Magnetospirillum* and have similar cell shape. Comparing results of rotational drag coefficient perpendicular to the cell long axis, we found that measurements return values of the rotational drag coefficients that are almost 50% higher than predicted by these simulations for all cell lengths. In addition, Pichel et al. 3D-printed macroscopic models of spiral cells and measured their rotational drag coefficient (perpendicular to cell longitudinal axis) at low Reynolds number [69]. They found that their printed spiral model cells had a $64 \pm 5\%$ higher drag than spheroid models with the same length and diameter. Comparing the power law fit of our experimental data (Fig. 3.9a red curve) with the theoretical predication for an ellipsoid (Fig. 3.9a black curve), the power fit is 59 – 64% higher than the theoretical predication for the ellipsoid in the range of average cell length ($L \approx 2.8 - 4.6\mu\text{m}$). Thus, our results coincides with

their finding.

Thirty two *E. coli* cells with average length of $2.5 \pm 0.6 \mu\text{m}$ with normal bundles swimming in motility buffer were studied by Darnton et al., and the average translational drag coefficient obtained was $f_t = 11 \pm 4 \text{ fN}\cdot\mu\text{m}\cdot\text{s}$, which is comparable to our result for cells around $3\mu\text{m}$ in length [70]. The average rotational drag coefficient obtained from their data is $f_{r\parallel} = 37 \pm 20 \text{ fN}\cdot\mu\text{m}/\text{s}$, which is also close to our result for cells with length around $3\mu\text{m}$. The shape difference between *E. coli* (ellipsoid) and the MTB we used (corkscrew shape) could cause the slight difference in drag coefficient values.

Chapter 4

Growing Magnetotactic Bacteria in Confined Environments

To continue our work on observing *Magnetospirillum magneticum* cells, we are planning to study their growth and division. The growth of more common lab strains such as *E. coli* has been studied and many groups have used microfluidic devices to study cell size change in order to investigate how cells control their size and maintain size homeostasis [71, 72]. Cellular division is especially interesting in the case of MTB, because it includes the sharing of the magnetosome chain between two daughter cells. In order to study the cells for a long period of time, we need to keep them in a confined space. We tried two devices: polydimethylsiloxane (PDMS) nanowells and PDMS microchannel combined with a gel membrane. PDMS, also known as dimethylpolysiloxane or dimethicone, is the most widely used silicon-based organic polymer. It is optically clear, and, in general, inert, and non-toxic. The PDMS nanowells and PDMS microchannels were kindly given by Dr. P. Ravi Selvaganapathy of McMaster University.

4.1 PDMS nanowells

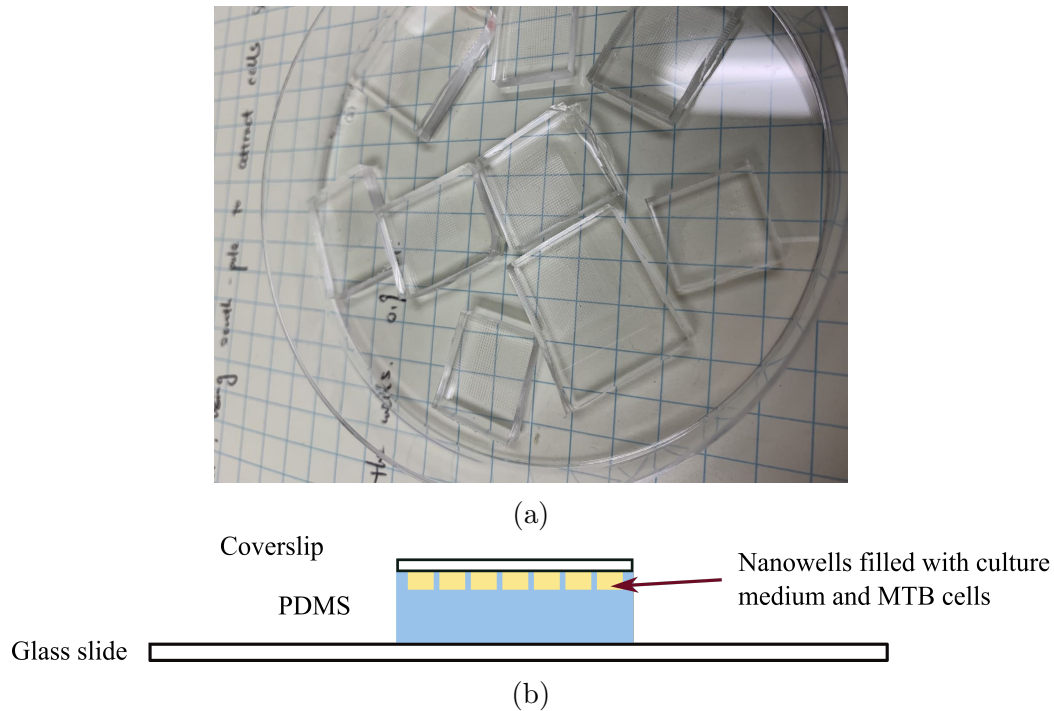


Figure 4.1: PDMS nanowell device. (a) A picture of PDMS nanowells before filling and assembly with the glass slide and coverslip. (b) Schematic representation of a PDMS nanowell device ready to be imaged.

The PDMS base and crosslinker were mixed in a 10 : 1 ratio. The mixture was poured onto the nanowell mould after the mixture being vacuumed to remove air bubbles. The mould was then placed on an 80°C leveled hot plate for 12 hours. Once fully cured, the PDMS was cut and peeled from the master mould. The PDMS is naturally hydrophobic, thus, its surface properties needed to be altered before the wells could be filled with bacteria culture. Plasma (partially ionized gas) treatment was done to render the wall of the wells hydrophilic. After this process, the nanowells were ready for experiments (Fig. 4.1a). We simply placed a glass slide under the PDMS, put one drop of bacteria culture on the PDMS surface and filled the wells by

swiping the solution back and forth with another glass slide. Then, with a coverslip on top and vacuum grease around the edge of the coverslip, the device was ready to be imaged (Fig. 4.1b).

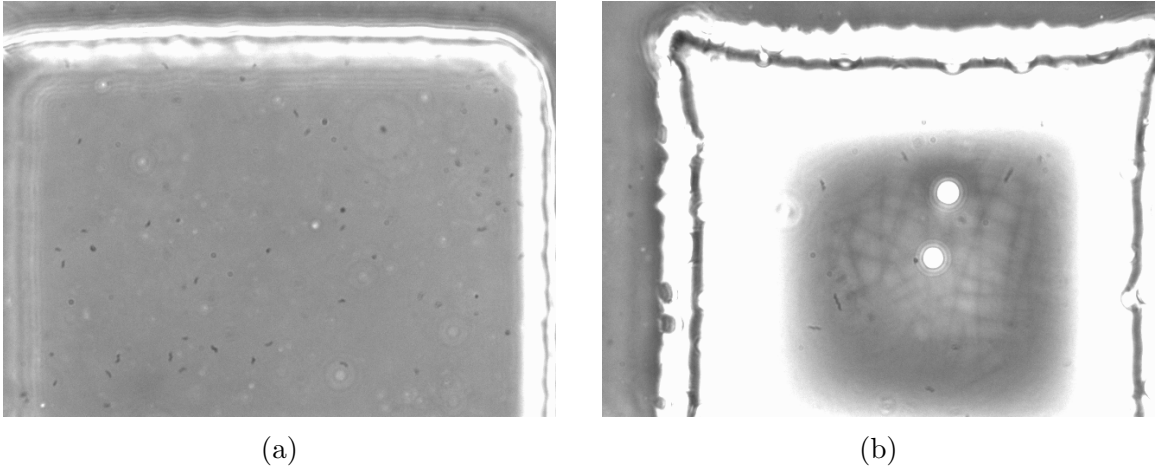


Figure 4.2: PDMS nanowell shape change. (a) A microscopy image of a single PDMS nanowell just after assembly. (b) A microscopy image of the same PDMS nanowell one day later.

We first tried three different sizes of wells, all of them were squares, with a depth of $100\ \mu\text{m}$, and a width of either 1, 0.5 or 0.3 mm. We filled the wells, incubated them at the optimal temperature (30°C) and checked the wells after a day. Most of the medium in the 1 and 0.5 mm wells had evaporated. The 0.3 mm wells had evaporation on the edge, but comparatively less than the bigger size wells. In addition, the 0.3 mm wells best fitted our camera field of view. Thus, we chose the 0.3 mm wells for further experiments. The evaporation killed the bacteria (the cells cannot survive without liquid or nutrients) and changed the shape of the PDMS wells (not ideal for imaging) (Fig. 4.2). To reduce the evaporation, we considered leaving the wells in the room instead of the incubator ($T_{room} < 30^\circ\text{C}$). The cells were growing faster in the incubator as expected, but at room temperature, the cells still grew and the shape of

the well changed slower. Thus, we chose to leave the wells in the room.

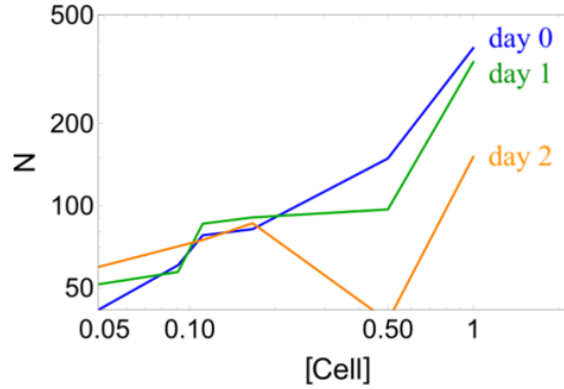


Figure 4.3: Number of cells in a single well vs. the relative cell concentration of the solution used to fill the wells on day 0. The blue curve is the data acquired on day 0, the green curve is day 1 data and the red curve is day 2 data.

The next thing we considered was the cell concentration in the wells. On the one hand, the cell density shouldn't be too high, as we want to image individual cells; on the other hand, if the cell density is too low, the cells will be hard to find and might not survive. We therefore tracked cell numbers in the nanowells over time for different initial cell concentrations, and the results are shown in Fig. 4.3. In Fig. 4.3, the x - axis is the relative cell concentration in the solution used to fill the nanowells, which depends on the dilution of the original culture, and for the y - axis, we have the number of cells in one region of a well obtained using ImageJ. We recorded a movie without changing the focus, then averaged the movie to get a background image, and subtracted the background image from every image in the movie. Finally the cells in the field of view were detected using Analyze Particles under Analyze menu. The cell number was then obtained by averaging the cell number detected in each frame. This method was not giving the exact number of live cells in the culture since we were focusing on only one layer and dead cells were counted as well, but it gives us a useful

relative cell number. When using a lower initial concentration of cells, their survival rate in the nanowells seemed to be higher (cell number continued increasing over the course of 3 days), presumably because nutrients were not depleted. We ended up with using relative cell concentration $[\text{Cell}] = 0.05 - 0.1$, where cells survived longer (Fig. 4.3).

With all conditions optimized, we started to observe the cells in the wells. We found that most of the cells were dead in the wells after a day, and the ones which survived tended to be long (Fig. 4.2 and Fig. 4.4). The death of most of the cells and longer cells' survival implies that the environment is not ideal (longer cells implies that they are not dividing). As mentioned before, AMB-1 cells are microaerophilic bacteria, but PDMS is O_2 permeable, which could result in O_2 levels higher than ideal in the wells. Another thing is the evaporation, which could make the cells uncomfortable. In addition, since we are not adding nutrients after leaving the cells in the wells, they might lack nutrients after a while. Or the cells dislike confined environments.

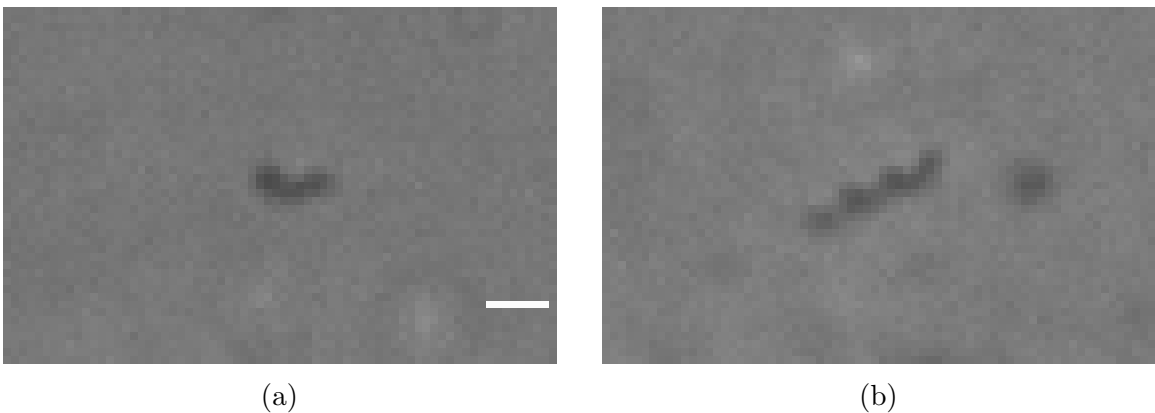


Figure 4.4: Images of cells in the wells. (a) A microscopy image of a representative cell on day 0 with $3 \mu\text{m}$ scale bar. (b) A microscopy image of a representative cell on day 1.

4.2 PDMS microchannel with a gel membrane

Because the MTB cells did not grow well in the PDMS nanowells, we tried a different device consisting of a PDMS microchannel stacked onto a gel membrane (Fig. 4.5). Using this device, instead of keeping the cells in a confined space, we immobilized the cells while hopefully keeping them alive in order to observe them for a long period of time. Here, the PDMS microchannel was used to provide continuous nutrients to the cells, and the hydrogel enabled cellular growth into a 2D monolayer (Fig. 4.5).

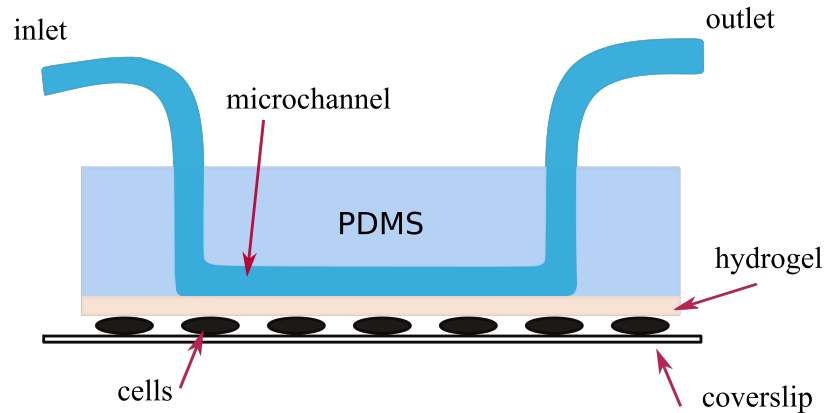


Figure 4.5: Schematic representation of PDMS microchannel with a gel membrane.

The PDMS microchannel was made following the same process as the PDMS nanowells using a channel master mould. In addition, after pouring the PDMS onto the master mould, two small tubes were inserted into the PDMS acting as the inlet and outlet during experiments. The hydrogel was made of agar powder (0.375 g) mixed with deionized water (DI water) (22.5 mL) [73]. The mixture was repeatedly microwaved for several seconds until the agar was completely dissolved. Then the mixture was injected into a warm custom-made chamber, which was made of two glass slides separated by three slices of parafilm strips ($\approx 350 \mu\text{m}$) on each end. The

chamber was then immediately submerged into fresh MTB growth medium to solidify the gel. Once the gel was solid, one glass slide was removed, and two drops of bacterial culture were placed on the hydrogel. After a few minutes, when the hydrogel had absorbed some bacterial solution, a coverslip was placed on the hydrogel (the side with bacteria). The chamber was then flipped, thus the coverslip was at the bottom, and the other glass slide forming the chamber could be removed. The PDMS microchannel was connected to a syringe pump with fresh medium, and after simply stacking the PDMS microchannel on top of the gel (Fig. 4.5), we started the pump to have a flow of medium.

Using an inverted microscope (Nikon Eclipse TS 100), we can image the channel and the cells embedded on the surface of the hydrogel (Fig. 4.6). However, by simply stacking the PDMS channel and the gel, we had a problem of leakage of the medium between the gel and the channel. The condition of the gel (how hydrated) may be important when attaching these two, because if the gel is too wet, the gel will easily move away from the channel; on the other hand, if the gel is too dry, it will be hard to attach them completely and the cells might be dead. In addition, the optimal flow rate of the medium needs to be determined, since a high flow rate could impact the seal between the channel and the gel, and the gel may dry out at a low flow rate. Combining this device with time-lapse microscopy, we plan to take long movies (~ 12 hours) to observe cell size change over time. Hopefully, we can obtain cell division time and cell length growth rate from the long movies. To study how the magnetosome chain is shared between two daughter cells, we would need to add a magnetic field just after cell division to see whether the two daughter cells have their magnetic moment in the same direction.

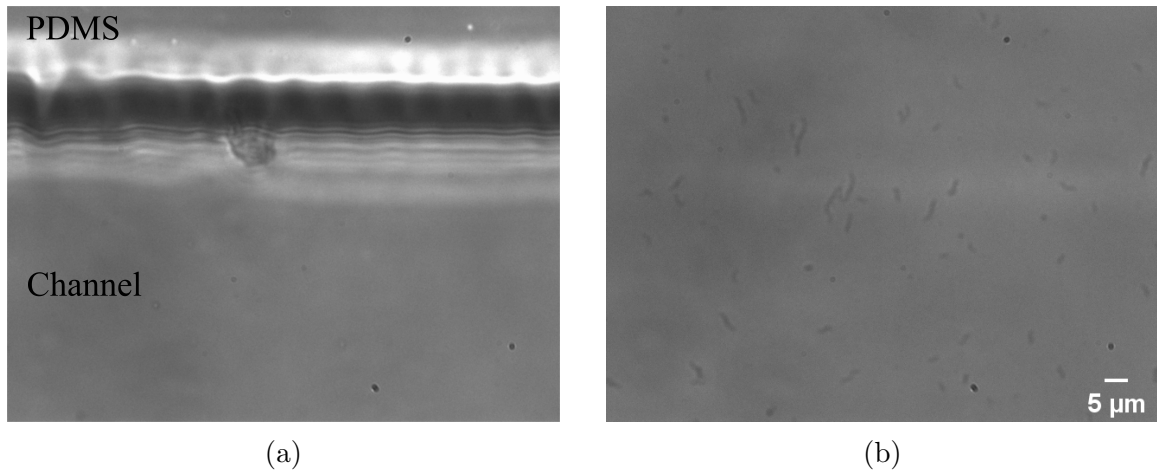


Figure 4.6: Images of the microchannel and cells embedded on the gel surface. (a) A microscopy image of the boundary of the microchannel. (b) A microscopy image of cells embedded on hydrogel.

Chapter 5

Conclusion

Drag coefficients are important parameters to fully understand the motility of microswimmers. We are interested in the magnetotactic species *Magnetospirillum magneticum*, with the characteristic "corkscrew" shape. The drag coefficients of spiral bacteria have been approximated by treating the cells as spheres [74], linear chains of spheres [75], cylinders [76, 35] and prolate spheroids [77]. A more accurate model was obtained by taking the actual helical shape of the cells into account using finite element analysis [68]. In addition, a group used 3D-printed macroscopic models of spiral cells and measured their rotational drag coefficients at low Reynolds number [69]. However, none of these approaches, accounts for the exact cellular shape or for the presence of flagella.

We proposed a way to experimentally measure the four principal drag coefficients of spirillum *M. magneticum* cells by recording their translational and rotational diffusion as observed with light microscopy. We took advantage of the helical shape, which allows a full determination of a cell's orientation from its projection in the focal plane [41, 78]. We also took advantage of the magnetic property of *M. magneticum*, which

allows roughly aligning the cell longitudinal axis with the external magnetic field and separately measuring transversal and longitudinal drag coefficients. We found the preferred experimental conditions and determined the analysis methods to extract different drag coefficients by simulating an elongated rigid magnetic particle diffusing in external magnetic fields. From experiments, we found that *M. magneticum* cells have a similar diffusion behavior as a cylinder and different shape parameters matter for different diffusions. For rotational diffusion, the overall shape of the cell is more important, but for the translational diffusion, the exact cell radius ($0.27\ \mu\text{m}$) (Fig. 2.8 “r”) dominates the diffusion behavior. As expected for a chiral object, we found a strong coupling between translational along and rotation around the cell longitudinal axis. Our results for the drag coefficients would permit a better modeling of the swimming motions of helical cells.

Once the challenges of leakage at the gel - PDMS channel interface and determination of the optimal flow rate are overcome, the device incorporating PDMS microchannel and hydrogel, with time-lapse microscopy, can hopefully be used to study cell growth, cell division and how the magnetosome chain is shared between two daughter cells.

Bibliography

- [1] Richard Blakemore. Magnetotactic bacteria. *Science*, 190(4212):377–379, 1975.
- [2] Richard B Frankel. The discovery of magnetotactic/magneto-sensitive bacteria. *Chinese Journal of Oceanology and Limnology*, 27(1):1, 2009.
- [3] Salvatore Bellini. On a unique behavior of freshwater bacteria. *Chinese Journal of Oceanology and Limnology*, 27(1):3, 2009.
- [4] Richard P Blakemore. Magnetotactic bacteria. *Annual Reviews in Microbiology*, 36(1):217–238, 1982.
- [5] Christopher T Lefèvre and Dennis A Bazylinski. Ecology, diversity, and evolution of magnetotactic bacteria. *Microbiol. Mol. Biol. Rev.*, 77(3):497–526, 2013.
- [6] Richard B Frankel, RP Blakemore, FF Torres De Araujo, Darci Motta S Esquivel, and J Danon. Magnetotactic bacteria at the geomagnetic equator. *Science*, 212(4500):1269–1270, 1981.
- [7] DA Bazylinski, CT Lefèvre, and D Schüler. Magnetotactic bacteria. *The prokaryotes*, pages 453–494, 2013.

- [8] Bruce M Moskowitz, Dennis A Bazylinski, Ramon Egli, Richard B Frankel, and Katrina J Edwards. Magnetic properties of marine magnetotactic bacteria in a seasonally stratified coastal pond (salt pond, ma, usa). *Geophysical Journal International*, 174(1):75–92, 2008.
- [9] Christopher T Lefevre, Fernanda Abreu, Marian L Schmidt, Ulysses Lins, Richard B Frankel, Brian P Hedlund, and Dennis A Bazylinski. Moderately thermophilic magnetotactic bacteria from hot springs in nevada. *Appl. Environ. Microbiol.*, 76(11):3740–3743, 2010.
- [10] Christopher T Lefèvre, Richard B Frankel, Mihály Pósfai, Tanya Prozorov, and Dennis A Bazylinski. Isolation of obligately alkaliphilic magnetotactic bacteria from extremely alkaline environments. *Environmental microbiology*, 13(8):2342–2350, 2011.
- [11] Christian Jogler, Gerhard Wanner, Sebastian Kolinko, Martina Niebler, Rudolf Amann, Nikolai Petersen, Michael Kube, Richard Reinhardt, and Dirk Schüler. Conservation of proteobacterial magnetosome genes and structures in an uncultivated member of the deep-branching nitrospira phylum. *Proceedings of the National Academy of Sciences*, 108(3):1134–1139, 2011.
- [12] Christopher T Lefèvre, Richard B Frankel, Fernanda Abreu, Ulysses Lins, and Dennis A Bazylinski. Culture-independent characterization of a novel, uncultivated magnetotactic member of the nitrospirae phylum. *Environmental microbiology*, 13(2):538–549, 2011.
- [13] Sebastian Kolinko, Christian Jogler, Emanuel Katzmann, Gerhard Wanner, Jörg

- Peplies, and Dirk Schüler. Single-cell analysis reveals a novel uncultivated magnetotactic bacterium within the candidate division op3. *Environmental microbiology*, 14(7):1709–1721, 2012.
- [14] Damien Faivre and Dirk Schuler. Magnetotactic bacteria and magnetosomes. *Chemical Reviews*, 108(11):4875–4898, 2008.
- [15] Dennis A Bazylinski, Richard B Frankel, Brigid R Heywood, Stephen Mann, John W King, Percy L Donaghay, and Alfred K Hanson. Controlled biomineralization of magnetite (Fe₃O₄) and greigite (Fe₃S₄) in a magnetotactic bacterium. *Appl. Environ. Microbiol.*, 61(9):3232–3239, 1995.
- [16] René Uebe and Dirk Schüler. Magnetosome biogenesis in magnetotactic bacteria. *Nature Reviews Microbiology*, 14(10):621, 2016.
- [17] Yorikane Fukuda, Yoshiko Okamura, Haruko Takeyama, and Tadashi Matsunaga. Dynamic analysis of a genomic island in magnetospirillum sp. strain amb-1 reveals how magnetosome synthesis developed. *FEBS letters*, 580(3):801–812, 2006.
- [18] Susanne Ullrich, Michael Kube, Sabrina Schübbe, Richard Reinhardt, and Dirk Schüler. A hypervariable 130-kilobase genomic region of magnetospirillum gryphiswaldense comprises a magnetosome island which undergoes frequent rearrangements during stationary growth. *Journal of bacteriology*, 187(21):7176–7184, 2005.

- [19] YURI A Gorby, TERRY J Beveridge, and RICHARD P Blakemore. Characterization of the bacterial magnetosome membrane. *Journal of Bacteriology*, 170(2):834–841, 1988.
- [20] DL Balkwill, D Maratea, and RP Blakemore. Ultrastructure of a magnetotactic spirillum. *Journal of Bacteriology*, 141(3):1399–1408, 1980.
- [21] Arash Komeili, Zhuo Li, Dianne K Newman, and Grant J Jensen. Magnetosomes are cell membrane invaginations organized by the actin-like protein mamK. *Science*, 311(5758):242–245, 2006.
- [22] Christian Jogler, Wei Lin, Anke Meyerdierks, Michael Kube, Emanuel Katzmann, Christine Flies, Yongxin Pan, Rudolf Amann, Richard Reinhardt, and Dirk Schüler. Toward cloning of the magnetotactic metagenome: identification of magnetosome island gene clusters in uncultivated magnetotactic bacteria from different aquatic sediments. *Appl. Environ. Microbiol.*, 75(12):3972–3979, 2009.
- [23] Michael Richter, Michael Kube, Dennis A Bazylinski, Thierry Lombardot, Frank Oliver Glöckner, Richard Reinhardt, and Dirk Schüler. Comparative genome analysis of four magnetotactic bacteria reveals a complex set of group-specific genes implicated in magnetosome biomineralization and function. *Journal of bacteriology*, 189(13):4899–4910, 2007.
- [24] Yao Ding, Jinhua Li, Jiangning Liu, Jing Yang, Wei Jiang, Jiesheng Tian, Ying Li, Yongxin Pan, and Jilun Li. Deletion of the *ftsZ*-like gene results in the production of superparamagnetic magnetite magnetosomes in magnetospirillum gryphiswaldense. *Journal of bacteriology*, 192(4):1097–1105, 2010.

- [25] Frank D Müller, Oliver Raschdorf, Hila Nudelman, Maxim Messerer, Emanuel Katzmann, Jürgen M Plitzko, Raz Zarivach, and Dirk Schüler. The ftsz-like protein ftszm of magnetospirillum gryphiswaldense likely interacts with its generic homolog and is required for biomineralization under nitrate deprivation. *Journal of bacteriology*, 196(3):650–659, 2014.
- [26] Isabel Kolinko, Anna Lohße, Sarah Borg, Oliver Raschdorf, Christian Jogler, Qiang Tu, Mihály Pósfai, Eva Tompa, Jürgen M Plitzko, Andreas Brachmann, et al. Biosynthesis of magnetic nanostructures in a foreign organism by transfer of bacterial magnetosome gene clusters. *Nature nanotechnology*, 9(3):193, 2014.
- [27] Donna E Goldhawk, Claude Lemaire, Cheryl R McCreary, Rebecca McGirr, Savita Dhanvantari, R Terry Thompson, Rene Figueredo, Jim Koropatnick, Paula Foster, and Frank S Prato. Magnetic resonance imaging of cells over-expressing maga, an endogenous contrast agent for live cell imaging. *Molecular imaging*, 8(3):7290–2009, 2009.
- [28] Lei Yan, Shuang Zhang, Peng Chen, Hetao Liu, Huanhuan Yin, and Hongyu Li. Magnetotactic bacteria, magnetosomes and their application. *Microbiological research*, 167(9):507–519, 2012.
- [29] Lei Yan, Huiyun Da, Shuang Zhang, Viviana Morillo López, and Weidong Wang. Bacterial magnetosome and its potential application. *Microbiological research*, 203:19–28, 2017.
- [30] Sylvain Martel, Charles C Tremblay, Serge Ngakeng, and Guillaume Langlois. Controlled manipulation and actuation of micro-objects with magnetotactic bacteria. *Applied Physics Letters*, 89(23):233904, 2006.

- [31] Chang-You Chen, Chuan-Fang Chen, Yong Yi, Lin-Jie Chen, Long-Fei Wu, and Tao Song. Construction of a microrobot system using magnetotactic bacteria for the separation of staphylococcus aureus. *Biomedical microdevices*, 16(5):761–770, 2014.
- [32] Michael R Benoit, Dirk Mayer, Yoram Barak, Ian Y Chen, Wei Hu, Zhen Cheng, Shan X Wang, Daniel M Spielman, Sanjiv S Gambhir, and A Matin. Visualizing implanted tumors in mice with magnetic resonance imaging using magnetotactic bacteria. *Clinical Cancer Research*, 15(16):5170–5177, 2009.
- [33] Tadashi Matsunaga, Toshifumi Sakaguchi, and Fumihiko Tadakoro. Magnetite formation by a magnetic bacterium capable of growing aerobically. *Applied Microbiology and Biotechnology*, 35(5):651–655, 1991.
- [34] Shimyoung Seong and Tai Hyun Park. Swimming characteristics of magnetic bacterium, magnetospirillum sp. amb-1, and implications as toxicity measurement. *Biotechnology and bioengineering*, 76(1):11–16, 2001.
- [35] Rohan Nadkarni, Solomon Barkley, and Cécile Fradin. A comparison of methods to measure the magnetic moment of magnetotactic bacteria through analysis of their trajectories in external magnetic fields. *PloS one*, 8(12), 2013.
- [36] Jinhua Li, Yongxin Pan, Guanjun Chen, Qingsong Liu, Lanxiang Tian, and Wei Lin. Magnetite magnetosome and fragmental chain formation of magnetospirillum magneticum amb-1: transmission electron microscopy and magnetic observations. *Geophysical Journal International*, 177(1):33–42, 2009.

- [37] Lucas Le Nagard, Viviana Morillo-López, Cecile Fradin, and Dennis A Bazylinski. Growing magnetotactic bacteria of the genus magnetospirillum: strains msr-1, amb-1 and ms-1. *JoVE (Journal of Visualized Experiments)*, (140):e58536, 2018.
- [38] MJ Smith, PE Sheehan, LL Perry, K OConnor, LN Csonka, BM Applegate, and LJ Whitman. Quantifying the magnetic advantage in magnetotaxis. *Biophysical journal*, 91(3):1098–1107, 2006.
- [39] David Le Sage, Koji Arai, David R Glenn, Stephen J DeVience, Linh M Pham, Lilah Rahn-Lee, Mikhail D Lukin, Amir Yacoby, Arash Komeili, and Ronald L Walsworth. Optical magnetic imaging of living cells. *Nature*, 496(7446):486–489, 2013.
- [40] A Krichevsky, MJ Smith, LJ Whitman, MB Johnson, TW Clinton, LL Perry, BM Applegate, K OConnor, and LN Csonka. Trapping motile magnetotactic bacteria with a magnetic recording head. *Journal of applied physics*, 101(1):014701, 2007.
- [41] Lucas Le Nagard, Liu Yu, Murtuza Rajkotwala, Solomon Barkley, Dennis A Bazylinski, Adam P Hitchcock, and Cécile Fradin. Misalignment between the magnetic dipole moment and the cell axis in the magnetotactic bacterium magnetospirillum magneticum amb-1. *Physical biology*, 16(6):066008, 2019.
- [42] Edward M Purcell. Life at low reynolds number. *American journal of physics*, 45(1):3–11, 1977.

- [43] Stephen Childress. *Mechanics of swimming and flying*, volume 2. Cambridge University Press, 1981.
- [44] Eric Lauga and Thomas R Powers. The hydrodynamics of swimming microorganisms. *Reports on Progress in Physics*, 72(9):096601, 2009.
- [45] Jonathon Howard et al. Mechanics of motor proteins and the cytoskeleton. 2001.
- [46] Henry Shum. Microswimmer propulsion by two steadily rotating helical flagella. *Micromachines*, 10(1):65, 2019.
- [47] Stefan Klumpp, Christopher T Lefèvre, Mathieu Bennet, and Damien Faivre. Swimming with magnets: From biological organisms to synthetic devices. *Physics Reports*, 789:1–54, 2019.
- [48] Howard C Berg. How bacteria swim. *Scientific American*, 233(2):36–45, 1975.
- [49] Howard C Berg and Robert A Anderson. Bacteria swim by rotating their flagellar filaments. *Nature*, 245(5425):380–382, 1973.
- [50] Dorothee Murat, Marion Hérisse, Leon Espinosa, Alicia Bossa, François Alberto, and Long-Fei Wu. Opposite and coordinated rotation of amphitrichous flagella governs oriented swimming and reversals in a magnetotactic spirillum. *Journal of bacteriology*, 197(20):3275–3282, 2015.
- [51] Graeme Lowe, Markus Meister, and Howard C Berg. Rapid rotation of flagellar bundles in swimming bacteria. *Nature*, 325(6105):637–640, 1987.
- [52] Howard C Berg and Linda Turner. Torque generated by the flagellar motor of escherichia coli. *Biophysical journal*, 65(5):2201–2216, 1993.

- [53] Xiaobing Chen and Howard C Berg. Torque-speed relationship of the flagellar rotary motor of escherichia coli. *Biophysical journal*, 78(2):1036–1041, 2000.
- [54] Richard B Frankel. Magnetic guidance of organisms. *Annual review of biophysics and bioengineering*, 13(1):85–103, 1984.
- [55] RS Wolfe, RK Thauer, and N Pfennig. A capillary racetrackmethod for isolation of magnetotactic bacteria. *FEMS Microbiology Ecology*, 3(1):31–35, 1987.
- [56] Joe Pogliano, Kit Pogliano, David S Weiss, Richard Losick, and Jon Beckwith. Inactivation of ftsi inhibits constriction of the ftsz cytokinetic ring and delays the assembly of ftsz rings at potential division sites. *Proceedings of the National Academy of Sciences*, 94(2):559–564, 1997.
- [57] Emanuel Katzmann, Frank D Müller, Claus Lang, Maxim Messerer, Michael Winklhofer, Jürgen M Plitzko, and Dirk Schüler. Magnetosome chains are recruited to cellular division sites and split by asymmetric septation. *Molecular microbiology*, 82(6):1316–1329, 2011.
- [58] Nazli Maki, Jason E Gestwicki, Ellen M Lake, Laura L Kiessling, and Julius Adler. Motility and chemotaxis of filamentous cells of escherichia coli. *Journal of Bacteriology*, 182(15):4337–4342, 2000.
- [59] Caroline A Schneider, Wayne S Rasband, and Kevin W Eliceiri. Nih image to imagej: 25 years of image analysis. *Nature methods*, 9(7):671–675, 2012.
- [60] Jonathan Saragosti, Pascal Silberzan, and Axel Buguin. Modeling e. coli tumbles by rotational diffusion. implications for chemotaxis. *PloS one*, 7(4):e35412, 2012.

- [61] Davide Giacché, Takuji Ishikawa, and Takami Yamaguchi. Hydrodynamic entrapment of bacteria swimming near a solid surface. *Physical Review E*, 82(5):056309, 2010.
- [62] PB Hylemon, JS Wells Jr, NR Krieg, and HW Jannasch. The genus spirillum: a taxonomic study1. *International Journal of Systematic and Evolutionary Microbiology*, 23(4):340–380, 1973.
- [63] Francis Perrin. Mouvement brownien d’un ellipsoide (ii). rotation libre et dépolarisation des fluorescences. translation et diffusion de molécules ellipsoïdales. *Journal de Physique et le Radium*, 7(1):1–11, 1936.
- [64] Yilong Han, Ahmed M Alsayed, Maurizio Nobili, Jian Zhang, Tom C Lubensky, and Arjun G Yodh. Brownian motion of an ellipsoid. *Science*, 314(5799):626–630, 2006.
- [65] Mikiji Miyata, Norimitsu Tohnai, and Ichiro Hisaki. Supramolecular chirality in crystalline assemblies of bile acids and their derivatives; three-axial, tilt, helical, and bundle chirality. *Molecules*, 12(8):1973–2000, 2007.
- [66] H Schmitzer, M Henstridge, D Engle, W Dultz, and D Tierney. Optical trapping of magnetic helical bacteria.
- [67] Hisanori Konishi and Zensaku Yoshii. Determination of the spiral conformation of aquaspirillum spp. by scanning electron microscopy of elongated cells induced by cephalixin treatment. *Microbiology*, 132(4):877–881, 1986.
- [68] Christina Zahn, Steve Keller, Mauricio Toro-Nahuelpan, Philipp Dorscht, Wolfgang Gross, Matthias Laumann, Stephan Gekle, Walter Zimmermann, Dirk

- Schüler, and Holger Kress. Measurement of the magnetic moment of single magnetospirillum gryphiswaldense cells by magnetic tweezers. *Scientific Reports*, 7(1):1–14, 2017.
- [69] MP Pichel, TAG Hageman, ISM Khalil, A Manz, and L Abelman. Magnetic response of magnetospirillum gryphiswaldense observed inside a microfluidic channel. *Journal of magnetism and magnetic materials*, 460:340–353, 2018.
- [70] Nicholas C Darnton, Linda Turner, Svetlana Rojevsky, and Howard C Berg. On torque and tumbling in swimming escherichia coli. *Journal of bacteriology*, 189(5):1756–1764, 2007.
- [71] Sattar Taheri-Araghi, Serena Bradde, John T Sauls, Norbert S Hill, Petra Anne Levin, Johan Paulsson, Massimo Vergassola, and Suckjoon Jun. Cell-size control and homeostasis in bacteria. *Current biology*, 25(3):385–391, 2015.
- [72] Yu Tanouchi, Anand Pai, Heungwon Park, Shuqiang Huang, Rumen Stamatov, Nicolas E Buchler, and Lingchong You. A noisy linear map underlies oscillations in cell size and gene expression in bacteria. *Nature*, 523(7560):357–360, 2015.
- [73] Jeong Wong, Shota Atsumi, Wei-Chih Huang, Tung-Yun Wu, Taizo Hanai, Miu-Ling Lam, Ping Tang, Jian Yang, James C Liao, and Chih-Ming Ho. An agar gel membrane-pdms hybrid microfluidic device for long term single cell dynamic study. *Lab on a Chip*, 10(20):2710–2719, 2010.
- [74] Darci Motta S Esquivel and Henrique GP Lins De Barros. Motion of magnetotactic microorganisms. *Journal of experimental biology*, 121(1):153–163, 1986.

- [75] AS Bahaj, PAB James, and FD Moeschler. An alternative method for the estimation of the magnetic moment of non-spherical magnetotactic bacteria. *IEEE Transactions on Magnetics*, 32(5):5133–5135, 1996.
- [76] AT Chwang, TY Wu, and H Winet. Locomotion of spirilla. *Biophysical Journal*, 12(11):1549–1561, 1972.
- [77] Mathias Reufer, Rut Besseling, Jana Schwarz-Linek, Vincent A Martinez, Alexander N Morozov, Jochen Arlt, Denis Trubitsyn, FB Ward, and Wilson CK Poon. Switching of swimming modes in magnetospirillum gryphiswaldense. *Biophysical journal*, 106(1):37–46, 2014.
- [78] Maira A Constantino, Mehdi Jabbarzadeh, Henry C Fu, and Rama Bansil. Helical and rod-shaped bacteria swim in helical trajectories with little additional propulsion from helical shape. *Science advances*, 2(11):e1601661, 2016.